Supplemental Table 3 The primers used for real-time RT-PCR in this study

Genes	Primers (forward/reverse; 5' to 3')
CK7	AGACGGAGTTGACAGAGCTG/GGATGGCCCGGTTCATCTC
CK19	CTCCCGCGACTACAGCCACT/TCAGCTCATCCAGCACCCTG
HES1	ATGGAGAAAAATTCCTCGTCCC/TTCAGAGCATCCAAAATCAGTGT
SOX9	TTTCCAAGACACAAACATGA/AAAGTCCAGTTTCTCGTTGA
integrin β4	GCAGCTTCCAAATCACAGAGG/CCAGATCATCGGACATGGAGTT
TO	GGCAGCGAAGAAGACAAATC/TCGAACAGAATCCAACTCCC
αAT	ACTGTCAACTTCGGGGACAC/CATGCCTAAACGCTTCATCA
ALB	GCACAGAATCCTTGGTGAACAG/ATGGAAGGTGAATGTTTTCAGCA
TGFBR2	GGAAACTTGACTGCACCGTT/CTGCACATCGTCCTGTGG
c/EBPα	TTCACATTGCACAAGGCACT/GAGGGACCGGAGTTATGACA
c/EBPβ	CGTGTACACACGCGTTCAG/CTCTCTGCTTCTCCCTCTGC
HNF6	CAAACCCTGGAGCAAACTCAA/TGTGTTGCCTCTATCCTTCCC
HNF1β	ACCAAGCCGGTCTTCCATACT/GGTGTGTCATAGTCGTCGCC
CYP2D6	CTTTCGCCCCAACGGTCTC/TTTTGGAAGCGTAGGACCTTG
TIR	TCATCGTCTGCTCCTCCTCT/AGGTGTCATCAGCAGCCTTT
HNF1α	AACACCTCAACAAGGGCACTC/CCCCACTTGAAACGGTTCCT
CYP3A4	AAGTCGCCTCGAAGATACACA/AAGGAGAGAACACTGCTCGTG
mouse αAT	TTGCTCGACACAACATGGAAT/ACGTCCCAGTTTGACATCTCT
mouse CYP7A1	GCTGTGGTAGTGAGCTGTTG/GTTGTCCAAAGGAGGTTCACC
mouse AQP1	AGGCTTCAATTACCCACTGGA/CTTTGGGCCAGAGTAGCGAT
mouse integrin β4	AGAGCTGTACCGAGTGCATC/TGGTGTCGATCTGGGTGTTCT

Supplemental Table 4 The primers used for ChIP assay in this study

	Primers (forward/reverse; 5' to 3')
c/EBP binding site A	TCACAACTTTCTAAGTCCCAATTTT/ACTGAGGCAGGGACTGTGTC
c/EBP binding site B	AACTGAAATGTCTTCCTTTTTCAA/CAGGAGGAGTAGAGCCAGCA
c/EBP binding site C	GCCACATTGTGTTTTCAGGA/ TTAGCCGAGAATGATGTCACC
c/EBP binding site D	CCAGAGGGCTGTACAGAATCA/ CCAGATTTGCCCAAGACATT
c/EBP binding site E	TGCCTACTGGGTGCTAGAGG/AACCTTCAGAGACAGCGATCA
β-actin	CCGGCGGGGTCTTTGTCTGAGC/GGGCCGGCCGCGTTATTACCA

OPEN ACCESS Freely available online

PLOS ONE

Prediction of Detailed Enzyme Functions and Identification of Specificity Determining Residues by Random Forests

Chioko Nagao[1]*, Nozomi Nagano[2], Kenji Mizuguchi[1]*

1 National Institute of Biomedical Innovation, Ibaraki, Osaka, Japan, **2** Computational Biology Research Center, AIST, Koto-ku, Tokyo, Japan

Abstract

Determining enzyme functions is essential for a thorough understanding of cellular processes. Although many prediction methods have been developed, it remains a significant challenge to predict enzyme functions at the fourth-digit level of the Enzyme Commission numbers. Functional specificity of enzymes often changes drastically by mutations of a small number of residues and therefore, information about these critical residues can potentially help discriminate detailed functions. However, because these residues must be identified by mutagenesis experiments, the available information is limited, and the lack of experimentally verified specificity determining residues (SDRs) has hindered the development of detailed function prediction methods and computational identification of SDRs. Here we present a novel method for predicting enzyme functions by random forests, EFPrf, along with a set of putative SDRs, the random forests derived SDRs (rf-SDRs). EFPrf consists of a set of binary predictors for enzymes in each CATH superfamily and the rf-SDRs are the residue positions corresponding to the most highly contributing attributes obtained from each predictor. EFPrf showed a precision of 0.98 and a recall of 0.89 in a cross-validated benchmark assessment. The rf-SDRs included many residues, whose importance for specificity had been validated experimentally. The analysis of the rf-SDRs revealed both a general tendency that functionally diverged superfamilies tend to include more active site residues in their rf-SDRs than in less diverged superfamilies, and superfamily-specific conservation patterns of each functional residue. EFPrf and the rf-SDRs will be an effective tool for annotating enzyme functions and for understanding how enzyme functions have diverged within each superfamily.

Citation: Nagao C, Nagano N, Mizuguchi K (2014) Prediction of Detailed Enzyme Functions and Identification of Specificity Determining Residues by Random Forests. PLoS ONE 9(1): e84623. doi:10.1371/journal.pone.0084623

Editor: Valerie de Crécy-Lagard, University of Florida, United States of America

Received June 27, 2013; **Accepted** November 15, 2013; **Published** January 8, 2014

Funding: This study was supported by the Industrial Technology Research Grant Program in 2007 (grant number 07C46056a) from New Energy and Industrial Technology Development Organization (NEDO) of Japan, Grants-in-Aid for Scientific Research from the Ministry of Education, Culture, Sports, Science, and Technology (grant numbers 25430186 and 25293079) and from the Ministry of Health, Labor, and Welfare to K.M., and also by Grant-in-Aid for Publication of Scientific Research Results (grant numbers 238048 and 248047) from Japan Society for the Promotion of Science (JSPS) to N.N. The funders had no role in study design, data collection and analysis, decision to publish, or preparation of the manuscript.

Competing Interests: The authors have declared that no competing interests exist.

* E-mail: chio@nibio.go.jp (CN); kenji@nibio.go.jp (KM)

Introduction

Almost all chemical reactions in living organisms are catalyzed by enzymes [1]. For a thorough understanding of cellular processes, it is essential to determine enzyme functions, i.e., what types of reactions are catalyzed, and what chemical compounds are utilized as substrates or cofactors. Prediction of enzyme function is a longstanding problem and many methods have been developed. The targeted functional details range from the broadest classification level such as enzyme/non-enzyme discrimination to a highly specific scheme such as the four-digit Enzyme Commission (EC) numbers [2]. Also, different types of features have been used, such as sequence/structural similarities, physico-chemical properties of amino acids, specific sequence/structural motifs, and their combinations [3–12]. Furthermore, many methods have been proposed recently for large-scale prediction of protein functions defined by Gene Ontology (GO) terms [13]. However, the most widely used method for functional annotation remains the simplest one: the transfer of functions based on sequence similarity calculated by BLAST/PSI-BLAST [14,15], despite its known limitations [16–19]. Moreover, predicting a precise enzyme function is still a significant challenge, as only a few methods currently available can predict the full four-digit EC numbers. The knowledge of such detailed functions can help determine true substrates for disease-related enzymes and design specific inhibitors for drug targets.

Enzymes in a protein family are considered to be evolutionary related. In many cases, these enzymes have similar but different functions. Divergence of sequences and functions are different in each family. Some enzymes, which share the sequence identity of over 90%, have different functions and differ in the first-digit of their EC numbers [16–19]. On the other hand, some enzymes, the sequence identity of which is below 30%, share all four digits of the EC numbers. This nonlinear correlation between function and sequence similarity makes the identification of detailed functions of enzymes such a difficult task.

One solution to overcome this problem is to use the information about functionally critical residues. The construction and use of sequence motifs can be considered an example of this approach [20,21]. Residues critical for functions, mutations of which bring drastic changes in the catalytic efficacy or substrate specificity, are sometimes called specificity determining residues (SDRs) or

function determining residues (FDRs). Proper information about SDRs is expected to improve the ability to distinguish enzyme functions [22–24]. However, such information is limited, because SDRs are determined by mutagenesis experiments. Therefore, most prediction methods use other properties serving as a proxy for SDRs [4,6,23–26]: catalytic residues, ligand binding sites or residues conserved in a functional subfamily. The lack of information about SDRs has hindered the development of computational methods for identifying SDRs [27–30] as well as predicting detailed functions.

Some machine learning methods can construct classifiers from a large number of attributes and calculate contributions from each attribute. Random forests [31] are one of the most accurate machine learning algorithms used for many applications, including the analysis of microarray data [32,33] and prediction of protein-protein interactions [34,35]. For enzyme function prediction, random forests have been applied for assigning the first or second digit of the EC numbers [7,8,36,37]. These methods used several hundreds of physico-chemical features calculated from only the full-length sequences and thus, provided no information about the importance of each residue for discriminating different functions.

In this study, we applied random forests, for the first time, for predicting the four-digit EC numbers (rather than only the first or second digit) in each homologous superfamily and also for obtaining a putative set of SDRs at the same time by using residue position specific attributes. We focus on a problem of discriminating detailed enzyme functions within a single protein family, since methods for assigning a protein sequence to an existing family have been well established. Thus, we assume that a functionally unknown protein has been already classified into a known protein family by sequence similarity. Given this framework, our objectives were two-fold; first, we aimed to develop a method that can predict the full four-digit EC number for a given protein. Second, we aimed to define putative SDRs as the most highly contributing positions used in our prediction model. Characterizing these "computational defined SDRs" in a systematic manner should mitigate the lack of experimentally defined SDRs.

Our analysis is based on the CATH domain classification [38]; we created a dataset from the UniProtKB/Swiss-Prot database [39] by selecting the enzymes, which had complete four-digit EC numbers and for which CATH homologous superfamilies were assigned by Gene3D [40]. For each enzyme in each superfamily, binary predictors were constructed by random forests with full-length sequence similarities and the residue similarities for active sites, ligand binding sites and conserved sites as input attributes. From the most highly contributing attributes, we obtained a set of putative SDRs and termed them random forests derived SDRs (rf-SDRs). The predictors (EFPrf) showed a performance comparable to that of a related method currently available and the rf-SDRs included many residues, for which functional importance had been verified by experimental studies. This study revealed a general tendency that functionally diverged superfamilies tend to include more active site residues (ASRs) in their rf-SDRs than in less diverged superfamilies. From the analysis of selected superfamilies, we also made superfamily-specific observations that conserved residues across enzymes, even if functionally important, tend not to be selected as rf-SDRs.

Results and Discussion

Overview of the enzyme function prediction

Figure 1A describes an overview of the enzyme function prediction method by random forests (EFPrf). A query to the system is a domain sequence pre-assigned to a CATH homologous superfamily (indicated as CATH X.X.X.X in the figure) by Gene3D. We chose a CATH homologous superfamily as a unit of protein family because a structure-based classification scheme can capture more distant proteins than a sequence-based one. In CATH X.X.X.X superfamily, binary predictors for each enzyme have been developed (Figure 1B). In each predictor, the query is aligned to the representative sequence by the FUGUE software [41] with the structure environment-specific substitution tables (ESSTs). Based on the alignment, the similarity scores for the full-length sequence and at the functional sites are calculated for the input to the predictor.

Dataset construction

We selected the enzyme sequences from the UniProtKB/Swiss-Prot database, for which complete EC numbers are assigned, and obtained their CATH domain regions from the Gene3D database. After removing redundancies, predictors have been constructed for the enzymes that had ten or more sequences and had at least one other enzyme in the superfamily (with a total of ten or more sequences) as negative data (Figure 2; see Materials and Methods for more details). Thus, we have built predictors for 1121 enzymes distributed over 306 CATH superfamilies. The representative structures for each enzyme were selected from the CATH S-level representatives with the longest sequence length and the highest resolution. In each superfamily, 3.7 enzymes were selected for constructing predictors on average. In 89 superfamilies, a single predictor was constructed. Fifteen superfamilies contained more than ten enzyme predictors and the largest superfamily was the NAD(P)-binding Rossmann-like domain superfamily (CATH 3.40.50.720) with 65 predictors (Table S1 and Figure S1). All the superfamilies, for which at least one predictor was created, were included in the analysis below.

Additional information to BLAST score improved the precision of the prediction

To investigate whether the use of the information about functional residues improves prediction performance or not, we built two types of predictors. First, we created simple decision trees by C4.5 with the BLAST bit score for the top hit in each enzyme as an attribute ("the simple model"). Because BLAST scores are the most widely used measure for function transfer, the simple model served as our baseline for predicting enzyme functions. Next, we constructed a second set of predictors by random forests (EFPrf) with more attributes. Three scoring matrices, BLOSUM62 [42], position specific scoring matrices (PSSM) [43] and ESST-based structural profiles, were used to calculate the scores at the active site residues (ASRs), ligand binding residues (LBRs) and conserved residues (CSRs), in addition to the full-length scores. The resulting 12 ($=3\times4$) attributes and the BLAST score were used as input to the system.

In a cross-validated benchmark assessment (see Materials and Methods), we followed a previous study [4] and calculated the maximal test to training sequence identity (MTTSI) for each query, and evaluated the prediction performance for eight different MTTSI ranges separately. Figure 3 and Table S2 show recall and precision averaged in each of the eight MTTSI ranges. (The average was taken by using only the enzymes, for which precision or recall was defined in the given MTTSI range.) In Figure 3A, recall in all ranges shows no significant differences between the simple model and EFPrf. On the other hand, precision improved significantly by EFPrf, especially in the lowest MTTSI range, where distinguishing functions by sequence similarity alone is known to be difficult (Figure 3B). This result

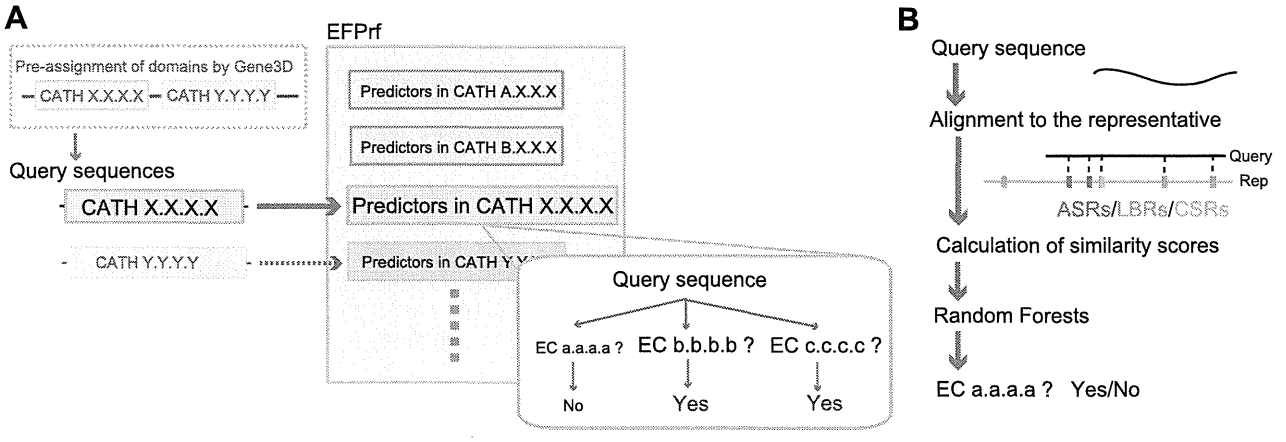

Figure 1. Outline of the EFPrf system (A) and the predictor for each enzyme constructed by Random Forests (B). A query to the system is a domain sequence pre-assigned to a CATH homologous superfamily by Gene3D. For each CATH superfamily, binary predictors, each for a known enzyme, process the query and return their results (A). In each predictor, the query is aligned to a representative sequence by the FUGUE software. Based on the alignment, similarity scores for the full-length sequence and at the functional sites are calculated for the input to the predictor (B).
doi:10.1371/journal.pone.0084623.g001

indicates that the additional information about functionally important residues is useful for discriminating detailed functions. Table 1 shows the prediction performance averaged over the 1121 enzyme predictors (see Table S3 for the individual values). Although a general trade-off between recall and precision was observed, the statistically significant increase in the F-measure achieved by EFPrf over the simple model also suggested the usefulness of the additional attributes of ASRs/LBRs/CSRs.

Because of differences in the training and test datasets, a direct comparison of performance with other methods is difficult but the prediction performance of EFPrf (recall = 0.30, precision = 0.78 in MTTSI <30%) is comparable to or better than that of EFICAz^2 [4,5] (recall = 0.23, precision = 0.74 in MTTSI <30%), which combines FDRs recognition, sequence similarity and support vector machine (SVM) models. Moreover, EFICAz^2 and EFPrf achieved an average precision of above 0.9 for MTTSI ≥40%, which is considered to be a "non trivial achievement" [4,17].

General properties of the random forest derived SDRs

In constructing the EFPrf, importance scores for each attribute were also calculated. We selected the top $3\times\sqrt{n}$ attributes as "highly contributing attributes", where n is the number of input attributes for each enzyme, and defined the residue positions in the highly contributing attributes (except for the full-length sequence similarity score) as the "random forests derived SDRs" (rf-SDRs) (Table S4). (In all enzymes, the full-length sequence similarity score was included in the highly contributing attributes, consistent with the result that the simple model was a modestly successful predictor.) On average, 8.4 residue positions were selected as the rf-SDRs for each enzyme. Among the position specific attributes calculated with different scoring matrices, the most frequently selected were those with PSSMs, suggesting that PSSMs may represent the amino acid differences among enzymes having similar structures/functions more clearly than the other scoring matrices (Table S5).

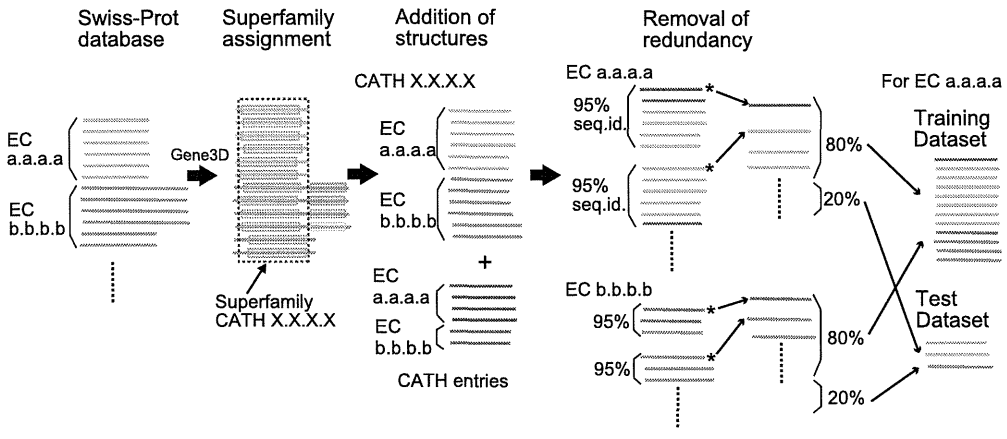

Figure 2. Outline of dataset construction. From the UniProtKB/Swiss-Prot database, the enzyme sequences, for which complete EC numbers are assigned, were obtained and their CATH domain regions from the Gene3D database were selected. After adding CATH entries and removal of redundancies, the enzymes having less than ten sequences were removed. The representative structures for each enzyme were selected from the CATH S-level representatives. In the remaining sequences, a predictor was constructed for an enzyme, which has sufficient numbers of positive and negative sequences (see Materials and Methods for more details). Randomly selected 80% of the sequences were used for training. The remaining 20% of the sequences were used as a test dataset.
doi:10.1371/journal.pone.0084623.g002

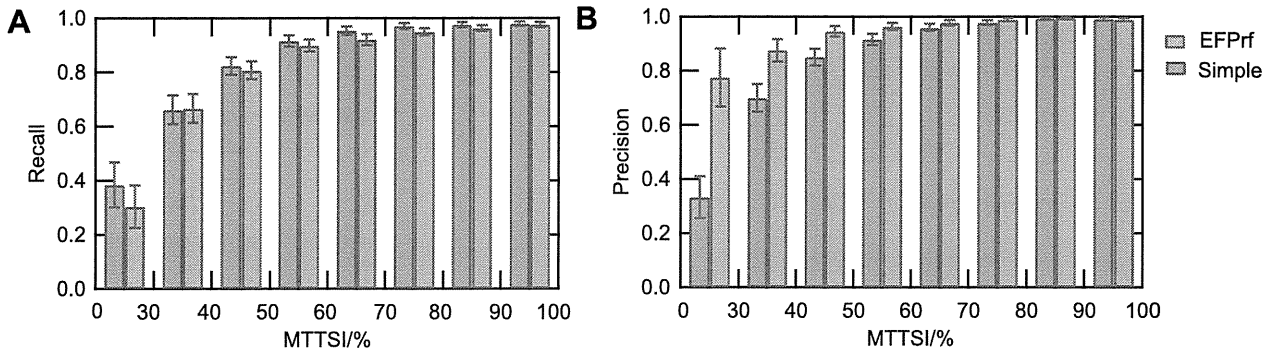

Figure 3. Prediction performance of EFPrf. The recall (A) and precision (B) at each level of the maximal test to training sequence identity (MTTSI) are plotted for the simple model (red) and the EFPrf (blue). Error bars represent 95% confidence intervals in each MTTSI range.
doi:10.1371/journal.pone.0084623.g003

Figure 4 shows the amino acid propensity for the rf-SDRs. The propensity of amino acid *i* was obtained as the fraction of amino acid *i* in the rf-SDRs divided by the fraction of amino acid *i* in all representative enzyme domains. In general, polar or charged residues were overrepresented in the rf-SDRs and non-polar residues were underrepresented. In polar, aromatic and charged residues, Trp, Tyr, Cys, Asn, Arg and His had a particularly high propensity value and in non-polar hydrophobic residues, Ala, Val, Leu and Ile had a low propensity value. In charged residues, Lys and Glu were underrepresented. This biased distribution of charged residues suggests that the delocalized charge in the guanidino group of Arg may be better utilized for SDRs than the charge in Lys, as observed in protein-protein interactions [44], and that the short side chain of Asp, with a smaller degree of freedom than that for Glu, is more suitable to form specific interactions. Some of the propensity values are different from those observed in the Catalytic Site Atlas (CSA) [45]; Asn favored for non-catalytic sites in the CSA [46], was overrepresented in the rf-SDRs and Lys and Glu, favored for catalytic sites in the CSA, were underrepresented. These differences are likely due to different definitions of functional residues, because the rf-SDRs were selected from not only catalytic sites but also ligand binding and conserved sites.

To analyze the relationships between functional diversity and the residues important for distinguishing functions, we classified superfamilies based on the functional entropy, defined by using the number of distinct EC numbers up to the third- and forth-digit levels (see details in Materials and Methods; Table S6). In the third-digit level classification, the three classes defined, the low-, medium- and high-degrees of functional diversity, approximately corresponded to having one, two to four, and more than four distinct EC numbers at the third-digit level within each superfamily. In the fourth-digit level classification, the low-, medium- and high-degrees of diversity corresponded to having one to five, six to ten and more than ten distinct EC numbers at the fourth-digit level within each superfamily. The prediction performance for the most diverged class was shown to be lower than that for the other classes in both the third- and fourth-digit based classification schemes (Tables S7 and S8).

Table 1. Prediction performance.

Model	Precision	Recall	F-measure
Simple	0.94	0.91	0.92
EFPrf	0.98 (<2.2e-16)	0.89 (1.3e-5)	0.93 (0.009)

The values in the parentheses represent the p-values calculated against the simple model by paired t-test.
doi:10.1371/journal.pone.0084623.t001

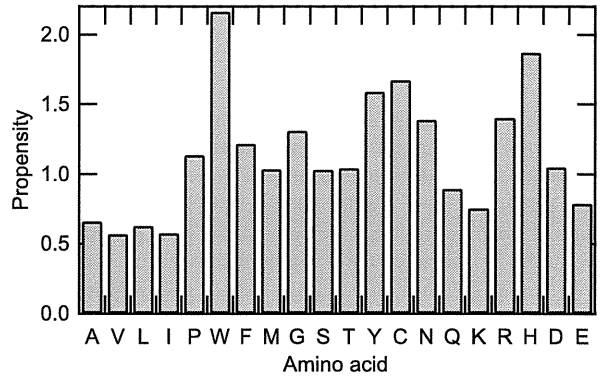

Figure 4. Amino acid propensities for the rf-SDRs. The propensity of amino acid *i* was calculated as the fraction of amino acid *i* in the rf-SDRs divided by the fraction of amino acid *i* in all representative enzyme domains.
doi:10.1371/journal.pone.0084623.g004

We then decided to examine what proportion of the ASRs or LBRs were selected as rf-SDRs in each superfamily. We excluded the CSRs from this analysis, because the ASRs and LBRs should be more directly linked to enzyme functions, whereas the identification of CSRs depended on the number of available sequences. If we consider all the superfamilies, the rf-SDRs included either no ASRs, about half of them or all of them (corresponding to peaks at zero, 0.5 and one in Figure S2), while in many superfamilies, about half of the LBRs were selected to be rf-SDRs (a peak around 0.5). We next examined these quantities as a function of functional diversity. Figure 5 and Table S9 showed that the proportion of ASRs to be selected as rf-SDRs increased with functional diversity, as defined by numbers of the third-digit EC number level functions. Although this tendency was weak (with moderate statistical significance for the difference; p-value = 0.019 for the superfamilies with low and medium functional diversity, and p-value = 0.017 for those with low and high functional diversity by the Wilcoxon rank sum test), it is consistent with the notion that enzymes in a superfamily with low functional diversity often have similar active sites and similar catalytic mechanisms and thus, ASRs generally do not distinguish different functions. On the other hand, the proportion of LBRs to be selected as rf-SDRs decreased slightly from medium to high functional diversity

but almost unchanged between low and high functional diversity, suggesting that LBRs can discriminate functions in superfamilies with all ranges of functional diversity. The same tendency was observed with functional diversity defined by numbers of the fourth-digit EC number level functions (Figure S3 and Table S10). The similar tendencies between the two classification schemes, observed in prediction performance and the proportions of ASRs and LBRs, may be accounted for by the observation that superfamilies with high functional diversity at the third-digit level generally have many distinct fourth digits in each third-digit EC number function.

Examples of superfamilies and enzymes

In this section, we describe a detailed investigation of the properties of the rf-SDRs in selected enzymes from superfamilies with different degrees of functional diversity. To remove potential biases associated with protein folds, we first show three superfamilies from a single fold, and next we show an additional example from a different fold. Only three folds, TIM barrel (CATH 3.20.20), α-βplaits (CATH 3.30.70) and Rossmann fold (CATH 3.40.50), satisfied the condition of having superfamilies in each of all three classes of functional diversity and in each class, containing at least one enzyme, for which the ASR information was available. From these three, we selected the TIM barrel fold (CATH 3.20.20). The TIM barrel, $(\alpha/\beta)_8$-barrel fold, is one of the largest and oldest fold and in the enzymes belonging to this fold, all the active sites are located at the C-terminal ends of the β-strands. As typical examples of superfamilies with low and high functional diversity, we chose glycosidases (CATH 3.20.20.80) and aldolase class I (CATH 3.20.20.70), respectively. We then chose phosphoenolpyruvate-binding domains (CATH 3.20.20.60) as an example of the superfamilies with medium functional diversity, although the number of enzymes with available ASR information was limited and the proportion of ASRs to be selected as rf-SDRs was somewhat atypical. Therefore, we additionally examined the α/β-hydrolase superfamily (CATH 3.40.50.1820) as a second example of the superfamilies with medium diversity, because this superfamily highlighted deviations from the average properties of this class of superfamilies explained by the well conserved catalytic triad.

Glycosidase superfamily (CATH 3.20.20.80). The glycosidase superfamily, where most enzymes belong to glycosidases (EC. 3.2.1), is a superfamily with low functional diversity. In our dataset, this superfamily contained 16 different glycosidases (EC 3.2.1) and three different hexosyltransferases (EC 2.4.1) (Table S3). The white bars in Figure 6 shows the distribution of the positions of the active site residues at eight C-terminal ends of the β-strands in this superfamily, highlighting three main catalytic residues at the β-strands 4, 7 and 6. This observation is consistent with the fact that 12 of the 16 glycosidases in this superfamily have been characterized as members of a group known as "the 4/7 group" [47–49]. (In the literature, this group is normally referred to as "the 4/7 superfamily" but to avoid confusion, we use the term group here.) The enzymes in the 4/7 group utilize two conserved catalytic acidic residues located at the C-terminal ends of β-strands 4 (acid/base) and 7 (nucleophile), as well as residues at the end of β-strand 6, which modulate the nucleophile. This biased distribution is reflected in the proportion of ASRs to be selected as rf-SDRs (32.7%), which was lower than the average for the

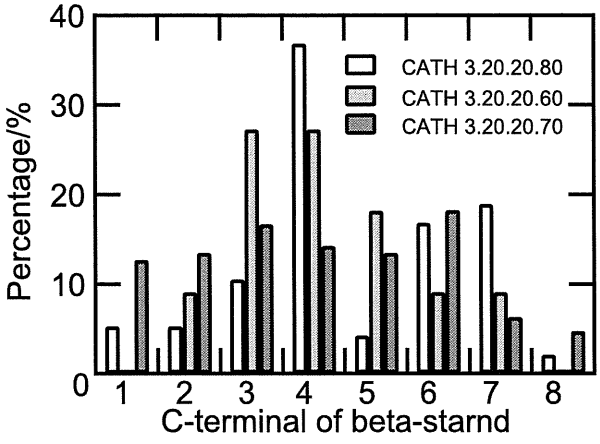

Figure 6. The distribution of active site residues at the end of eight β-strands of enzymes in the superfamilies adopting the TIM barrel fold. White bars represent the glycosidase superfamily (CATH 3.20.20.80), light gray bars represent the phosphoenolpyruvate-binding domain superfamily (CATH 3.20.20.60), and gray bars represent the aldolase class I superfamily (CATH 3.20.20.70). The percentages were calculated by using 18, three and 29 enzymes for glycosidases, phosphoenolpyruvate-binding domains and aldolase class I, respectively, for which active site information was available.
doi:10.1371/journal.pone.0084623.g006

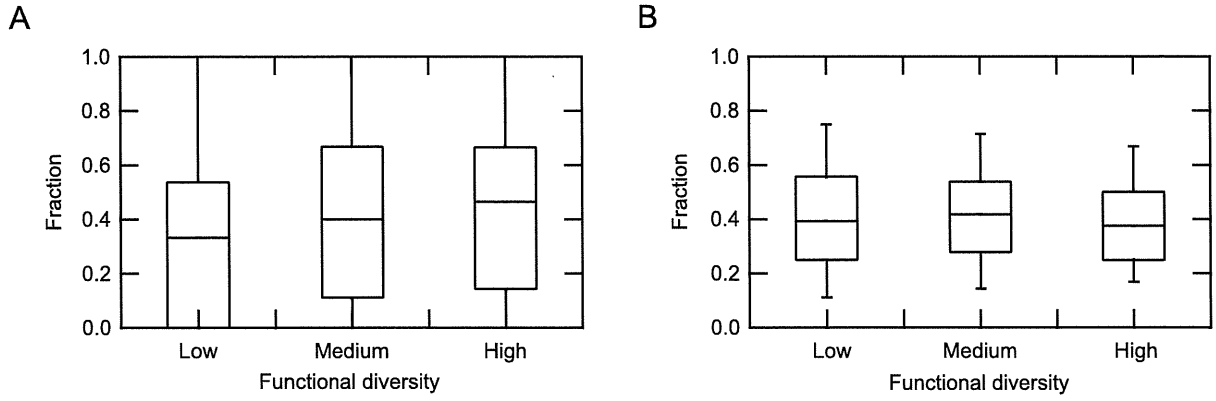

Figure 5. Distributions of fractions of the rf-SDRs in active site residues (ASRs, A) and ligand binding residues (LBRs, B), observed in the superfamilies with low, medium and high degrees of functional diversity classified at the third-digit level of EC numbers. The top and bottom of a box indicate 75th and 25th percentiles and the horizontal line in a box represents the median value. The top and bottom whiskers represent 90th and 10th percentiles.
doi:10.1371/journal.pone.0084623.g005

group of superfamilies with low functional diversity (35.0%), (Tables S9 and S11).

Figure 7 shows two example enzymes of the 4/7 group, endo-1,4-β-xylanase (EC 3.2.1.8, Figure 7A) and cellulase (EC 3.2.1.4, Figure 7B). In both enzymes, none of the two 4/7 catalytic residues (Glu 159, Glu 265 in Figure 7A and Glu 170, Glu 307 in Figure 7B, respectively) was selected as the rf-SDRs. The rf-SDRs included some residues on β-strand 6, His 236 in endo-1,4-β-xylanase and His 254 and Tyr 256 in cellulase, which contact the nucleophiles and are invariant in each enzyme but different between the two enzymes [50–52]. The proportion of ASRs to be selected as rf-SDRs in endo-1,4-β-xylanase is lower (0.25) than that in cellulase (0.5), possibly because the former enzyme share the active site residues (other than the 4/7 catalytic residues) with a larger number of other enzymes such as glucan 1,4-α-maltohydrolase (EC 3.2.1.133) and cyclomaltodextrin glucanotransferase (EC 2.4.1.19) than the latter enzyme.

The rf-SDRs also included some LBRs, which are located in similar spatial positions but not equivalent in the sequence alignment, His 95 (endo-1,4-β-xylanase) and His 122 (cellulase) [50] shown to be essential for ligand binding by mutagenesis experiments [53–55], and the residues critical for determining the substrate positions, Trp 241 at the +3 subsite [56], Asn 59 and Lys 62 at the -2 subsite [57], in endo-1,4-β-xylanase.

Aldolase class I superfamily (CATH 3.20.20.70). The Aldolase class I superfamily is known to be an old family including a variety of enzymes. In our dataset, predictors for 34 different enzymes were constructed in this superfamily (Table S3). These 34 enzymes included EC numbers with six different first-digits, showing the highest functional entropy in all the superfamilies. The ASR positions showed a broad distribution, indicating that the numerous functions are achieved by the active sites located at various ends of β-strands (Figure 6, dark gray bars). For instance, in 5-aminolevulinic acid dehydratase (ALADH, EC 4.2.1.24) [58], the catalytic Lys 195 and Lys 247 are positioned at the ends of β-7 and β-8, respectively and in phosphoribosylformimino-5-aminoimidazole carboxamide ribonucleotide (ProFAR) isomerase (HisA, EC 5.3.1.16) [59], the catalytic Asp 8 is positioned at the C-terminal end of β-1. Aldolase class I enzymes typically have substrates or cofactors with a phosphate-group, such as flavin mononucleotide (FMN), but enzymes in this superfamily also act on a variety of other substrates. The proportion of ASRs to be selected as rf-SDRs (51.9%) was higher than the average for the group of superfamilies with high functional diversity (43.7%) (Tables S9 and S11). This observation suggests that the ASRs located differently among the enzymes can be used effectively for discriminating different functions in this superfamily.

Figures 8A and 8B show the rf-SDRs of quinolinate phosphoribosyltransferase (hQPRTase; EC 2.4.2.19) and α-galactosidase (α-Gal; EC 3.2.1.22) as examples of enzymes having dissimilar functions. The rf-SDRs of hQPRTase included one core residue of the phosphate binding motif [60] Ala 268 at the end of β-10, which corresponds to β-8 in a conventional $(\alpha/\beta)_8$ barrel (in Figure 8A, the numbering of the β-strands based on the conventional barrel), and one of the catalytic residues, Lys 140 on β-1. Leu 170 and Lys 172 on β-4, the conformational change of which was suggested to be important for the specificity and reaction mechanism [61], were also included (Figure 8A). On the other hand, α-Gal recognizes the substrate having no phosphate moiety, mainly around the C-terminal ends of β-3 to β-6 [62]. In addition to the nucleophile Asp 130 at the end of β-4, many LBRs on these β-strands were selected as rf -SDRs (Figure 8B).

Figures 8C and 8D show ProFAR isomerase (HisA) (EC 5.3.1.16) and phosphoribosylanthranilate (PRA) isomerase (TrpF) (EC 5.3.1.24) as examples of enzymes having more similar functions. These enzymes catalyze the Amadori rearrangements of different substrates ProFAR and PRA by similar mechanisms [63,64]. These substrates share a ribose-5-phosphate moiety, and ProFAR has an additional ribose connected by imidazole and PRA has an anthranilate moiety. Also known are PriA, which can catalyze both reactions, and its close homologue subHisA, which lacks the TrpF activity [65].

In the rf-SDRs of HisA, the only known catalytic residue (Asp 8) was selected. In TrpF, the corresponding active site, Cys 7, was not selected and the reason is unclear. In LBRs, some residues interacting with different moieties of each substrate were selected to be rf-SDRs: Ser 34 and Arg 36 of TrpF, which interact with the anthranilate moiety of the substrate [66], Gly 20 and Leu 52 of HisA, which would interact with the imidazole and attached amide moieties (inferred from the homologous PriA structure). Additionally, the rf-SDRs included His 48 and Trp 138 of HisA, likely to be important for the catalytic activity for PRA (also

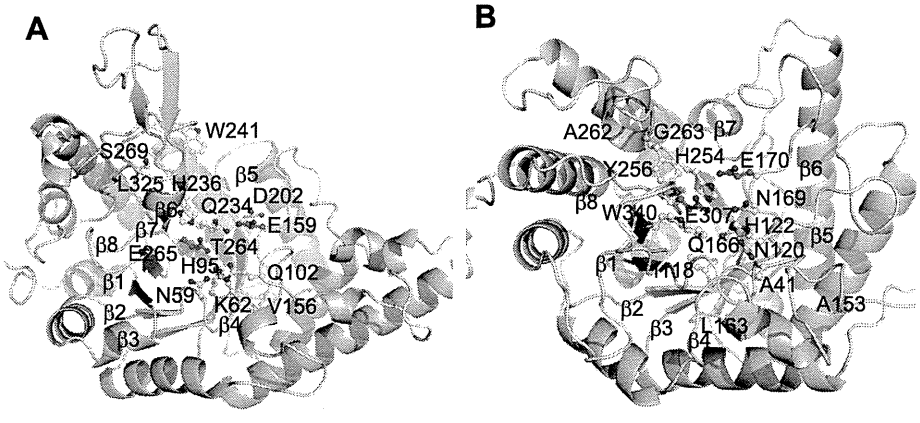

Figure 7. The rf-SDRs for (A) endo-1,4-xylanase (EC 3.2.1.8, CATH domain: 1r87A00) and (B) cellulase (EC 3.2.1.4, CATH domain: 1edgA00) in the glycosidase superfamily (CATH 3.20.20.80). The rf-SDRs are represented by balls and sticks, where nitrogen atoms are colored blue, oxygen atoms are red, sulfur atoms are yellow and carbon atoms are white. The carbon atoms of the active sites selected as rf-SDRs are colored magenta. Eight β-strands in a conventional barrel are colored blue, cyan, green, lemon, yellow, yelloworange, orange, and red, from the N-terminal to the C-terminal. In both enzymes, none of the two catalytic acid residues common in many enzymes in the superfamily, colored magenta, was selected.
doi:10.1371/journal.pone.0084623.g007

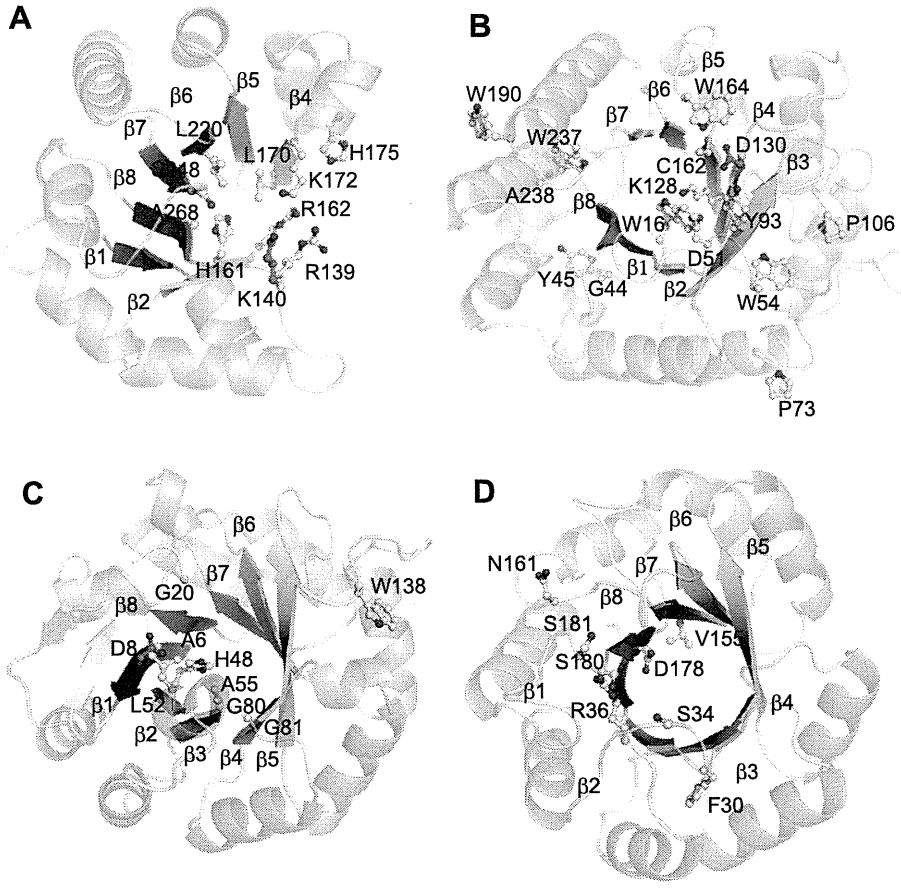

Figure 8. The rf-SDRs for (A) quinolinate phosphoribosyltransferase (hQPRTase; EC 2.4.2.19, CATH domain: 1qprF02), (B) α-galactosidase (α-Gal; EC 3.2.1.22, CATH domain: 1uasA01), (C) phosphoribosylformimino-5-aminoimidazole carboxamide ribonucleotide isomerase (HisA) (EC 5.3.1.16, CATH domain: 1qo2A00) and (D) phosphoribosylanthranilate isomerase (TrpF) (EC 5.3.1.24, CATH domain: 1nsjA00) in aldolase class I superfamily (CATH 3.20.20.70). The rf-SDRs are represented by balls and sticks, where nitrogen atoms are colored blue, oxygen atoms are red, sulfur atoms are yellow and carbon atoms are white. The carbon atoms of the active sites selected as rf-SDRs are colored magenta. Eight β-strands in a conventional barrel are colored blue, cyan, green, lemon, yellow, yelloworange, orange, and red, from the N-terminal to the C-terminal. The rf-SDRs in the figures A and B clearly show that the rf-SDRs for hQPRTase include the phosphate binding motif located in β-7 and β-8 in the conventional barrel structure but those for α-Gal are mainly located after β-1 to -5. The figure D shows the residues interacting with different moieties in substrates between HisA and TrpF, Ser 34 and Arg 36.
doi:10.1371/journal.pone.0084623.g008

inferred from the PriA structure) [67]. In addition to these residues, different residues in different enzymes were selected, from those interacting with common parts of the substrates such as the phosphate moiety.

Phosphoenolpyruvate-binding domain superfamily (CATH 3.20.20.60). The phosphoenolpyruvate-binding domain superfamily mainly consists of transferases (EC 2) and lyases (EC 4). Most of these enzymes have substrates or cofactors with a phosphate-moiety, while the phosphate binding sites are distributed over the C-terminal ends of β-strands 2 to 6. The predictors for six different enzymes consisting of two phosphotransferases with paired acceptors (EC 2.7.9), two oxo-acid-lyases (EC 4.1.3) and other transferases (EC 2) were constructed (Table S3). This superfamily was classified into the group of medium functional diversity.

Despite generally dissimilar active sites among these enzymes (Figure 6, light gray bars), the proportion of ASRs to be selected as rf-SDRs (23.5%) was lower than the average for the group of superfamilies with medium functional diversity (43.4%) (Tables S9 and S11). This result may be explained by the conservation of some of the active site residues. For example, pyruvate phosphate dikinase (EC 2.7.9.1) has the only known active site, Cys 831 [68] and this position in the alignment was also occupied by cysteine in pyruvate water dikinase (EC 2.7.9.2) (although no active site information is available for the latter enzyme). This position was not selected to be an rf-SDR, decreasing the average proportion of ASRs to be selected.

α/β-hydrolase superfamily (CATH 3.40.50.1820). α/β-hydrolase superfamily is one of the large superfamilies, containing a wide variety of enzymes such as carboxylic acid ester hydrolases, peptidases, lipid hydrolases and haloalkane dehalogenases. In our dataset, predictors for 13 enzymes were constructed (Table S3). All these enzymes shared the first digit of the EC number (EC3; hydrolases) and this superfamily belonged to the group of superfamilies with medium functional diversity. A variety of functions are achieved by the conserved catalytic triad: a nucleophile (Ser, Cys or Asp) positioned after β-5, an acidic residue after β-7 and histidine after the last β-8 strand, and the versatile substrate binding sties by insertions and deletions at the C-terminal ends ofβ-3, 4, 6, 7 or 8 [69,70]. Such a conserved catalytic triad and a similar chemical reaction mechanism are reflected in the proportion of ASRs to be selected as rf-SDRs

(26.2%), which was lower than the average value (43.4%) for the group of medium functional diversity (Tables S9 and S11).

For instance, acetylcholine esterase (AChE, EC 3.1.1.7) shown in Figure 9 has the conventional catalytic triad, Ser, Glu, and His, and a deep and narrow cavity around the catalytic site called "active site gorge" formed by large insertions, which is considered to determine the specificity for acetylcholine [71]. In 15 rf-SDRs, no residue of the catalytic triad was selected and about 40% of the rf-SDRs were located in the active site gorge. Trp 84 and Phe 330 are known as the anionic site to bind the choline moiety and Tyr 121, Trp 279 and Phe 290 are important for determining the gorge conformation [72–75]. Phe 290 causes steric hindrance with a large acyl group in the acyl pocket and plays a critical role in stabilizing the methyl moiety of acetylcholine [76].

These examples show whether each residue can be selected as an rf-SDR or not depends on whether it is conserved within a superfamily regardless of what roles the equivalent residues play in other enzymes. A residue may be conserved and used as a catalytic residue for the same chemical reaction in other enzymes and thus, it tends not to be selected as an rf-SDR, as observed in the glycosidase superfamily. A conserved residue may be used for catalyzing different chemical reaction but because of its conservation, it cannot be selected to be an rf-SDR, as observed in the α/β-hydrolase superfamily. In some superfamilies, different amino acid residues are used for catalyzing different chemical reactions or binding different ligands, in which case, these functional residues can be selected for rf-SDRs, as observed in the aldolase class I superfamily.

Conclusion

We have developed EFPrf, a novel method based on random forests for predicting enzyme functions at the fourth-digit level of the EC number in each CATH homologous superfamily. As input attributes, we used amino acid residue similarities at ASRs, LBRs and CSRs, in addition to similarity in the full-length sequence. The prediction performance of EFPrf improved significantly over the decision trees constructed using BLAST scores alone (the simple model), especially in the low MTTSI regions, where it is known to be difficult to distinguish detailed functions by sequence similarity alone. This observation suggested that the information about functionally important sites would be useful for predicting detailed functions. During the construction of EFPrf, we also obtained the rf-SDRs from the most highly contributing attributes. The analysis of the selected superfamilies showed that the rf-SDRs included many experimentally verified SDRs. Moreover, we showed that the rf-SDRs reflected the mechanisms of functional diversification within each superfamily; the rf-SDRs both indicate a general degree of functional diversity (as measured by the proportion of ASRs to be selected as rf-SDRs) and the specific characteristics of each superfamily represented by the conservations of each residue in a superfamily. Thus, EFPrf is a useful tool for predicting detailed enzyme functions and the rf-SDRs are a good resource for determining SDRs by experimental and computational methods and understanding functional diversity in a superfamily.

In this paper, we examined individual domain sequences preassigned to a CATH superfamily for validating EFPrf. In practice, enzyme sequences often consist of multiple domains and in the future, we will develop a method for combining prediction results for the individual domains of a query sequence and producing an overall function prediction. In recent years, many methods have been proposed for predicting protein functions described by GO terms [13]. Our method can be extended to GO term prediction and may be efficient in the low sequence similarity region, where GO terms are also difficult to predict [24,77].

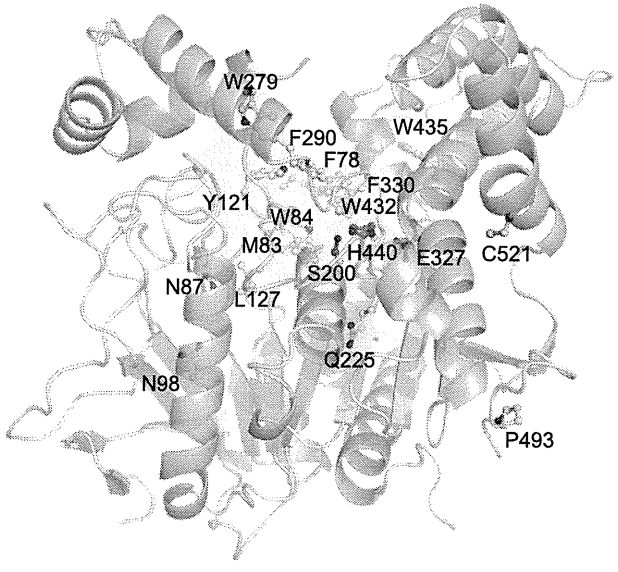

Figure 9. The rf-SDRs for acetylcholine esterase (AChE, EC 3.1.1.7, CATH domain: 1w76B00) in α/β-hydrolase superfamily (CATH 3.40.50.1820). The rf-SDRs are represented by balls and sticks, where carbon atoms are colored white, nitrogen atoms are blue, oxygen atoms are red and sulfur atoms are yellow. The active site gorge is partially represented by green surface. At the bottom of the active site gorge, the catalytic triads, which are not selected to be the rf-SDRs, are represented by balls and sticks and colored magenta. Many rf-SDRs are positioned around the catalytic gorge region.
doi:10.1371/journal.pone.0084623.g009

Materials and Methods

Dataset preparation

Figure 2 shows an outline of the dataset construction. From the UniProtKB/Swiss-Prot database [39] (release 2010_06), we selected the enzyme sequences that: i) had been annotated with complete four-digit EC numbers, ii) were not fragment sequences and iii) had domains assigned to CATH [38] superfamilies in the Gene3D database [40]. A total of 332,021 enzyme domain sequences were obtained. In the following, an enzyme sequence refers to a protein domain sequence thus created, which was associated with a single CATH superfamily. The domain sequences were treated as independent sequences, although some of these were obtained from single multi-domain proteins. In order to obtain structural information, the 72,993 enzymes in the CATH database (ver. 3.3) were added to the 332,021 enzyme sequences. In each enzyme (as distinguished by the four-digit EC number) in each superfamily, all these sequences were clustered at a 95% sequence identity cutoff by using blastclust [78]. Also for each enzyme, a single representative structure was selected as the CATH S-level representative structure with the longest sequence length and the highest resolution. In the 95%-identity cluster that included the representative structure, the corresponding sequence was considered the representative of the cluster and in the other 95%-identity clusters, the longest sequence was selected as the representative. After the removal of redundancy, 201,708 sequences remained.

In the remaining sequences, a predictor was constructed for an enzyme if: 1) the enzyme belonged to a superfamily that contained at least one other enzyme in it, 2) the enzyme had a representative

structure and ten or more sequences and 3) a total of ten or more sequences were available for the other enzymes as negative data in the superfamily. We randomly selected 80% of the sequences from a given enzyme and 80% of the sequences from the other enzymes in the superfamily for training. The remaining 20% of the sequences were used as a test dataset. A total of 1121 enzymes over 306 CATH homologous superfamilies were selected for benchmarking.

Calculations of attributes for classifiers

In addition to the BLAST [14,15] bit score, we used two types of scores as attributes: the scores calculated by using a full-length sequence and the scores at the functionally important positions in the alignment of a query sequence to a representative structure. The functionally important positions were defined to be the active sites, ligand binding sites and conserved site residues. In the following sections, we describe the selection of these positions and the score calculations.

Determination of the alignment positions used for attribute calculations. i) Active site and ligand binding residue positions from the literature and structural information: We obtained the literature information about active site residues from the Enzyme Catalytic-Mechanism Database (EzCatDB, ver. 20100722) [79] and the Catalytic Site Atlas (CSA, ver. 2.2.12) [45] database. All annotations in the EzCatDB and the original, hand-annotated entries derived from the primary literature in the CSA were used.

Ligand (substrate, cofactor, intermediate, products and their analogues) information in the Protein Data Bank (PDB) [80] was obtained from the EzCatDB and PROCOGNATE (ver. 1.6) [81] databases. All annotations in the EzCatDB and the cognate ligand entries with similarity scores higher than 0.5 in PROCOGNATE were used. Ligand binding residues were defined from complex structures by using LIGPLOT [82]. The residues that interacted with the ligands through both hydrogen bonds and hydrophobic interactions were considered as ligand binding residues. Ligand assignments to obsolete PDB entries were ignored.

We defined active site and ligand binding positions of each enzyme as the alignment positions, which were used by at least one PDB entry corresponding to that enzyme as an active site or a ligand-binding site, respectively. The position used as both active and ligand binding sites was defined to be an active site residue (ASR) position. The ASRs and ligand binding residues (LBRs) were mapped on to the representative structure for the calculation of attributes based on a multiple structural alignment, generated by MUSTANG [83], between the available complex structures and the representative.

ii) Conserved amino acid residue positions: For each enzyme in the training dataset, a multiple sequence alignment was generated by clustalw [84] and this alignment was aligned to the representative structure by FUGUE [41]. FUGUE performs sequence-structure comparison by utilizing environment-specific substitution tables (ESSTs). An ESST-based structural profile was calculated for the representative structure of each enzyme. To examine amino acid conservation, the entropy S_k for each alignment position k was calculated as

$$S_k = \sum_{i=1}^{21} -P^i \log P^i,$$

where i represents 20 types of amino acids plus a gap and P^i is the fraction of amino acid type i at this position. The top 10% conserved residue positions (CBRs) in one enzyme were selected for the calculation of attributes. The positions where the fraction of the gap was above 20% were excluded from the entropy calculation. If the positions selected as CBRs were already defined as ASRs or LBRs, those positions were defined to be ASRs or LBRs.

Position-specific scoring matrices (PSSMs) [43] were also calculated from the multiple sequence alignments. The PSSM scores at the ith alignment positions were given by

$$P_{ij} = \sum_{k=1}^{20} W_{ki} sim(k,j),$$

where i is the alignment position, j and k are the amino acid types and $sim(k, j)$ is the score in the BLOSUM 62 matrix between amino acid types j and k [42]. The logarithmic weight W_{ki} was defined, depending on occurrences of amino acid type k at position i, as

$$W_{ki} = \frac{\ln\left[1 - \left(\frac{\sum_{n=1}^{N} \delta_{ki}}{N+1}\right)\right]}{\ln\left(\frac{1}{N+1}\right)}, \quad \delta_{ki} = \begin{cases} 1, & \text{amio acid type is } k \\ 0, & \text{if amino acid type is not } k \end{cases},$$

where N is the number of sequences in the alignment.

Calculation of scores. Given a query sequence, a BLAST search was performed against the sequences in the training dataset for each enzyme in each superfamily. The bit score for the top hit was used as an attribute for the predictors (see below). In the training mode, the bit score for the top hit, except for its own sequence, was used.

The other attributes were calculated based on an alignment between the query sequence and the representative structure by using three different scoring matrices: BLOSUM62, ESSTs and PSSMs. The latter two matrices were specific to each enzyme, as described in the previous section. The full-length sequence scores and the scores at ASRs, LBRs and CBRs were calculated.

Construction of predictors and evaluation of performance

Decision trees were constructed by C4.5 [85] algorithms implemented in WEKA, a data mining software tool in Java (ver. 3.6.5) [86], with default parameters. Forests of decision trees were constructed by the random forests [31] algorithm implemented in R (ver. 2.15.1), a language and environment for statistical computing [87]. The default value was used for the number of attributes to split on at each node (floor($\sqrt{n}$), where n is the number of input attributes), since the number of attributes was different for each enzyme. The number of trees constructed for each classifier was set to be 500, by comparing averaged out-of-bag (OOB) error rates obtained from the models with 250, 500 and 750 trees (data not shown). In construction of random forest for each enzyme, the importance score for each attribute was calculated. We selected the top 3*floor($\sqrt{n}$) ranked attributes as highly contributing attributes, analyzed their properties and defined the associated residues as random forest-derived specificity determining residues (rf-SDRs).

In order to evaluate prediction performance in regions where sequence identities between test and training sequences are low, we calculated the maximal test to training sequence identity (MTTSI) following Arakaki *et al.* [4] (see the reference for the detailed definition of MTTSI). Table S12 shows the number of positive and negative sequences in each MTTSI bin of the test set.

Given a predictor for enzyme EC *a.a.a.a*, a set of prediction results were obtained (by using the test sequences) and these results were divided into eight bins according to their MTTSI values. Then for each bin, precision = TP/(TP+FP) and recall = TP/(TP+FN) were calculated, where TP is the number of true positives, FP is the number of false positives and FN is the number of false negatives. Finally, these precision and recall values were averaged over all the enzymes, for which it was possible to define the performance measure (i.e., (TP+FP) >0 for precision and (TP+FN) >0 for recall within a bin).

Functional entropy of a superfamily

For classifying superfamilies at the EC third-digit level, we defined the functional entropy S_{func} for each superfamily as follows:

$$P_{a.b.c} = \frac{n_{a.b.c}}{N},$$

$$S_{func} = \sum_{a.b.c} -P_{a.b.c} \ln P_{a.b.c}$$

where $n_{a.b.c.}$ is the number of predictors that share the first three digits of their EC numbers (*a.b.c*) and N is the total number of predictors in the superfamily. Using the functional entropy, superfamilies were classified into three groups: highly diverged ($1.5 \leq S_{func}$), moderately diverged ($0.5 \leq S_{func} < 1.5$) and least diverged ($0 \leq S_{func} < 0.5$). The cutoff values were determined such that the occurrences of distinct EC numbers at the third-digit level within each superfamily approximately corresponded to one, two to four, and more than four, respectively (data not shown).

Supporting Information

Figure S1 Distribution of the number of enzyme predictors constructed in a superfamily. The region between 20 to 70 is expanded and represented in the figure. Fifteen superfamilies contained more than ten enzyme predictors and the largest superfamily was NAD(P)-binding Rossmann-like domain superfamily (CATH 3.40.50.720) with 65 predictors.
(EPS)

Figure S2 Distribution of the active site residues (ASRs) and ligand binding residues (LBRs) in all superfamilies. The white bars represent the ASRs and the light gray bars represent the LBRs.
(EPS)

Figure S3 Distributions of fractions of the rf-SDRs in active site residues (ASRs, A) and ligand binding residues (LBRs, B), observed in the superfamilies with low, medium and high degrees of functional diversity classified at the fourth-digit level of EC numbers. The top and bottom of a box indicate 75th and 25th percentiles and the horizontal line in a box represents the median value. The top and bottom whiskers represent 90th and 10th percentiles.
(EPS)

Table S1 Number of predictors in each CATH homologous superfamily.
(XLSX)

Table S2 Precision and recall of enzymes in each MTTSI bin.
(DOCX)

Table S3 Prediction performance of each predictor.
(XLSX)

Table S4 List of the rf-SDRs.
(XLSX)

Table S5 Differences of scoring matrices selected in the rf-SDRs.
(DOCX)

Table S6 Classifications of superfamilies at the third- and forth-digit levels of EC numbers.
(XLSX)

Table S7 Averaged prediction performance for different classes of functional diversity at the third-digit level of EC numbers.
(DOCX)

Table S8 Averaged prediction performance for different classes of functional diversity at the forth-digit level of EC numbers.
(DOCX)

Table S9 The average proportion of ASRs/LBRs to be selected as rf-SDRs for different classes of functional diversity at the third-digit level of EC numbers.
(DOCX)

Table S10 The average proportion of ASRs/LBRs to be selected as rf-SDRs for different classes of functional diversity at the fourth-digit level of EC numbers.
(DOCX)

Table S11 The number of rf-SDRs in ASRs, LBRs and CSRs.
(DOCX)

Table S12 The number of positive and negative queries in each MTTSI bin.
(DOCX)

Author Contributions

Conceived and designed the experiments: CN KM. Performed the experiments: CN. Analyzed the data: CN KM. Contributed reagents/materials/analysis tools: CN NN KM. Wrote the paper: CN KM.

References

1. Voet D, Voet JG (1990) Biochemistry: John Wiley and Sons, New York.
2. Webb EC, NC-IUBMB (1992) Enzyme Nomenclature 1992, Recommendations of the Nomenclature Committee of the International Union of Biochemistry and Molecular Biology on the Nomenclature and Classification of Enzymes. San Diego, California: Academic Press.
3. Wass MN, Barton G, Sternberg MJ (2012) CombFunc: predicting protein function using heterogeneous data sources. Nucleic Acids Res 40: W466–470.
4. Arakaki AK, Huang Y, Skolnick J (2009) EFICAz2: enzyme function inference by a combined approach enhanced by machine learning. BMC Bioinformatics 10: 107.
5. Kumar N, Skolnick J (2012) EFICAz2.5: application of a high-precision enzyme function predictor to 396 proteomes. Bioinformatics 28: 2687–2688.
6. Redfern OC, Dessailly BH, Dallman TJ, Sillitoe I, Orengo CA (2009) FLORA: a novel method to predict protein function from structure in diverse superfamilies. PLoS Comput Biol 5: e1000485.
7. Kumar C, Choudhary A (2012) A top-down approach to classify enzyme functional classes and sub-classes using random forest. EURASIP J Bioinform Syst Biol 2012: 1.
8. Bray T, Doig AJ, Warwicker J (2009) Sequence and structural features of enzymes and their active sites by EC class. J Mol Biol 386: 1423–1436.
9. Shen HB, Chou KC (2007) EzyPred: a top-down approach for predicting enzyme functional classes and subclasses. Biochem Biophys Res Commun 364: 53–59.
10. Dobson PD, Doig AJ (2003) Distinguishing enzyme structures from non-enzymes without alignments. J Mol Biol 330: 771–783.
11. Laskowski RA, Watson JD, Thornton JM (2005) ProFunc: a server for predicting protein function from 3D structure. Nucleic Acids Res 33: W89–93.
12. Hulo N, Bairoch A, Bulliard V, Cerutti L, Cuche BA, et al. (2008) The 20 years of PROSITE. Nucleic Acids Res 36: D245–249.

13. Radivojac P, Clark WT, Oron TR, Schnoes AM, Wittkop T, et al. (2013) A large-scale evaluation of computational protein function prediction. Nat Methods 10: 221–227.
14. Altschul SF, Gish W, Miller W, Myers EW, Lipman DJ (1990) Basic local alignment search tool. J Mol Biol 215: 403–410.
15. Altschul SF, Madden TL, Schaffer AA, Zhang J, Zhang Z, et al. (1997) Gapped BLAST and PSI-BLAST: a new generation of protein database search programs. Nucleic Acids Res 25: 3389–3402.
16. Todd AE, Orengo CA, Thornton JM (2001) Evolution of function in protein superfamilies, from a structural perspective. J Mol Biol 307: 1113–1143.
17. Tian W, Skolnick J (2003) How well is enzyme function conserved as a function of pairwise sequence identity? J Mol Biol 333: 863–882.
18. Addou S, Rentzsch R, Lee D, Orengo CA (2009) Domain-based and family-specific sequence identity thresholds increase the levels of reliable protein function transfer. J Mol Biol 387: 416–430.
19. Rost B, Liu J, Nair R, Wrzeszczynski KO, Ofran Y (2003) Automatic prediction of protein function. Cell Mol Life Sci 60: 2637–2650.
20. Bannert C, Welfle A, Aus dem Spring C, Schomburg D (2010) BrEPS: a flexible and automatic protocol to compute enzyme-specific sequence profiles for functional annotation. BMC Bioinformatics 11: 589.
21. Claudel-Renard C, Chevalet C, Faraut T, Kahn D (2003) Enzyme-specific profiles for genome annotation: PRIAM. Nucleic Acids Res 31: 6633–6639.
22. Nagao C, Nagano N, Mizuguchi K (2010) Relationships between functional subclasses and information contained in active-site and ligand-binding residues in diverse superfamilies. Proteins 78: 2369–2384.
23. George RA, Spriggs RV, Bartlett GJ, Gutteridge A, MacArthur MW, et al. (2005) Effective function annotation through catalytic residue conservation. Proc Natl Acad Sci U S A 102: 12299–12304.
24. Wass MN, Sternberg MJ (2008) ConFunc—functional annotation in the twilight zone. Bioinformatics 24: 798–806.
25. Kristensen DM, Ward RM, Lisewski AM, Erdin S, Chen BY, et al. (2008) Prediction of enzyme function based on 3D templates of evolutionarily important amino acids. BMC Bioinformatics 9: 17.
26. Tian W, Arakaki AK, Skolnick J (2004) EFICAz: a comprehensive approach for accurate genome-scale enzyme function inference. Nucleic Acids Res 32: 6226–6239.
27. Capra JA, Singh M (2008) Characterization and prediction of residues determining protein functional specificity. Bioinformatics 24: 1473–1480.
28. Kalinina OV, Novichkov PS, Mironov AA, Gelfand MS, Rakhmaninova AB (2004) SDPpred: a tool for prediction of amino acid residues that determine differences in functional specificity of homologous proteins. Nucleic Acids Res 32: W424–428.
29. Lichtarge O, Bourne HR, Cohen FE (1996) An evolutionary trace method defines binding surfaces common to protein families. J Mol Biol 257: 342–358.
30. Addington Ta Fau - Mertz RW, Mertz Rw Fau - Siegel JB, Siegel Jb Fau - Thompson JM, Thompson Jm Fau - Fisher AJ, Fisher Aj Fau - Filkov V, et al. Janus: prediction and ranking of mutations required for functional interconversion of enzymes.
31. Breiman L (2001) Random Forests. Machine Learning Journal: 5–32.
32. Diaz-Uriarte R, Alvarez de Andres S (2006) Gene selection and classification of microarray data using random forest. BMC Bioinformatics 7: 3.
33. Svetnik V, Liaw A, Tong C, Culberson JC, Sheridan RP, et al. (2003) Random forest: a classification and regression tool for compound classification and QSAR modeling. J Chem Inf Comput Sci 43: 1947–1958.
34. Lee BJ, Shin MS, Oh YJ, Oh HS, Ryu KH (2009) Identification of protein functions using a machine-learning approach based on sequence-derived properties. Proteome Sci 7: 27.
35. Chen XW, Liu M (2005) Prediction of protein-protein interactions using random decision forest framework. Bioinformatics 21: 4394–4400.
36. Cai CZ, Han LY, Ji ZL, Chen YZ (2004) Enzyme family classification by support vector machines. Proteins 55: 66–76.
37. Syed U, Yona G (2009) Enzyme function prediction with interpretable models. Methods Mol Biol 541: 373–420.
38. Orengo CA, Michie AD, Jones S, Jones DT, Swindells MB, et al. (1997) CATH—a hierarchic classification of protein domain structures. Structure 5: 1093–1108.
39. UniProt Consortium (2012) Reorganizing the protein space at the Universal Protein Resource (UniProt). Nucleic Acids Res 40: D71–75.
40. Lees J, Yeats C, Redfern O, Clegg A, Orengo C (2010) Gene3D: merging structure and function for a Thousand genomes. Nucleic Acids Res 38: D296–300.
41. Shi J, Blundell TL, Mizuguchi K (2001) FUGUE: sequence-structure homology recognition using environment-specific substitution tables and structure-dependent gap penalties. J Mol Biol 310: 243–257.
42. Henikoff S, Henikoff JG (1992) Amino acid substitution matrices from protein blocks. Proc Natl Acad Sci U S A 89: 10915–10919.
43. Gribskov M, Luthy R, Eisenberg D (1990) Profile analysis. Methods Enzymol 183: 146–159.
44. Nagao C, Izako N, Soga S, Khan SH, Kawabata S, et al. (2012) Computational design, construction, and characterization of a set of specificity determining residues in protein-protein interactions. Proteins 80: 2426–2436.
45. Porter CT, Bartlett GJ, Thornton JM (2004) The Catalytic Site Atlas: a resource of catalytic sites and residues identified in enzymes using structural data. Nucleic Acids Res 32: D129–133.
46. Gutteridge A, Thornton JM (2005) Understanding nature's catalytic toolkit. Trends Biochem Sci 30: 622–629.
47. Henrissat B, Davies G (1997) Structural and sequence-based classification of glycoside hydrolases. Curr Opin Struct Biol 7: 637–644.
48. Nagano N, Porter CT, Thornton JM (2001) The (betaalpha)(8) glycosidases: sequence and structure analyses suggest distant evolutionary relationships. Protein Eng 14: 845–855.
49. Cantarel BL, Coutinho PM, Rancurel C, Bernard T, Lombard V, et al. (2009) The Carbohydrate-Active EnZymes database (CAZy): an expert resource for Glycogenomics. Nucleic Acids Res 37: D233–238.
50. Dominguez R, Souchon H, Spinelli S, Dauter Z, Wilson KS, et al. (1995) A common protein fold and similar active site in two distinct families of beta-glycanases. Nat Struct Biol 2: 569–576.
51. Ducros V, Czjzek M, Belaich A, Gaudin C, Fierobe HP, et al. (1995) Crystal structure of the catalytic domain of a bacterial cellulase belonging to family 5. Structure 3: 939–949.
52. Dominguez R, Souchon H, Lascombe M, Alzari PM (1996) The crystal structure of a family 5 endoglucanase mutant in complexed and uncomplexed forms reveals an induced fit activation mechanism. J Mol Biol 257: 1042–1051.
53. Bortoli-German I, Haiech J, Chippaux M, Barras F (1995) Informational suppression to investigate structural functional and evolutionary aspects of the Erwinia chrysanthemi cellulase EGZ. J Mol Biol 246: 82–94.
54. Navas J, Beguin P (1992) Site-directed mutagenesis of conserved residues of Clostridium thermocellum endoglucanase CelC. Biochem Biophys Res Commun 189: 807–812.
55. Belaich A, Fierobe HP, Baty D, Busetta B, Bagnara-Tardif C, et al. (1992) The catalytic domain of endoglucanase A from Clostridium cellulolyticum: effects of arginine 79 and histidine 122 mutations on catalysis. J Bacteriol 174: 4677–4682.
56. Zolotnitsky G, Cogan U, Adir N, Solomon V, Shoham G, et al. (2004) Mapping glycoside hydrolase substrate subsites by isothermal titration calorimetry. Proc Natl Acad Sci U S A 101: 11275–11280.
57. Charnock SJ, Lakey JH, Virden R, Hughes N, Sinnott ML, et al. (1997) Key residues in subsite F play a critical role in the activity of Pseudomonas fluorescens subspecies cellulosa xylanase A against xylooligosaccharides but not against highly polymeric substrates such as xylan. J Biol Chem 272: 2942–2951.
58. Erskine PT, Norton E, Cooper JB, Lambert R, Coker A, et al. (1999) X-ray structure of 5-aminolevulinic acid dehydratase from Escherichia coli complexed with the inhibitor levulinic acid at 2.0 A resolution. Biochemistry 38: 4266–4276.
59. Lang D, Thoma R, Henn-Sax M, Sterner R, Wilmanns M (2000) Structural evidence for evolution of the beta/alpha barrel scaffold by gene duplication and fusion. Science 289: 1546–1550.
60. Nagano N, Orengo CA, Thornton JM (2002) One fold with many functions: the evolutionary relationships between TIM barrel families based on their sequences, structures and functions. J Mol Biol 321: 741–765.
61. Sharma V, Grubmeyer C, Sacchettini JC (1998) Crystal structure of quinolinic acid phosphoribosyltransferase from Mmycobacterium tuberculosis: a potential TB drug target. Structure 6: 1587–1599.
62. Fujimoto Z, Kaneko S, Momma M, Kobayashi H, Mizuno H (2003) Crystal structure of rice alpha-galactosidase complexed with D-galactose. J Biol Chem 278: 20313–20318.
63. List F, Sterner R, Wilmanns M (2011) Related (betaalpha)8-barrel proteins in histidine and tryptophan biosynthesis: a paradigm to study enzyme evolution. Chembiochem 12: 1487–1494.
64. Reisinger B, Bocola M, List F, Claren J, Rajendran C, et al. (2012) A sugar isomerization reaction established on various (betaalpha)(8)-barrel scaffolds is based on substrate-assisted catalysis. Protein Eng Des Sel 25: 751–760.
65. Noda-Garcia L, Camacho-Zarco AR, Medina-Ruiz S, Gaytan P, Carrillo-Tripp M, et al. (2013) Evolution of Substrate Specificity in a Recipient's Enzyme Following Horizontal Gene Transfer. Mol Biol Evol 30: 2024–2034.
66. Henn-Sax M, Thoma R, Schmidt S, Hennig M, Kirschner K, et al. (2002) Two (betaalpha)(8)-barrel enzymes of histidine and tryptophan biosynthesis have similar reaction mechanisms and common strategies for protecting their labile substrates. Biochemistry 41: 12032–12042.
67. Due AV, Kuper J, Geerlof A, von Kries JP, Wilmanns M (2011) Bisubstrate specificity in histidine/tryptophan biosynthesis isomerase from Mycobacterium tuberculosis by active site metamorphosis. Proc Natl Acad Sci U S A 108: 3554–3559.
68. Nakanishi T, Nakatsu T, Matsuoka M, Sakata K, Kato H (2005) Crystal structures of pyruvate phosphate dikinase from maize revealed an alternative conformation in the swiveling-domain motion. Biochemistry 44: 1136–1144.
69. Nardini M, Dijkstra BW (1999) Alpha/beta hydrolase fold enzymes: the family keeps growing. Curr Opin Struct Biol 9: 732–737.
70. Holmquist M (2000) Alpha/Beta-hydrolase fold enzymes: structures, functions and mechanisms. Curr Protein Pept Sci 1: 209–235.
71. Sussman JL, Harel M, Frolow F, Oefner C, Goldman A, et al. (1991) Atomic structure of acetylcholinesterase from Torpedo californica: a prototypic acetylcholine-binding protein. Science 253: 872–879.
72. Harel M, Kryger G, Rosenberry TL, Mallender WD, Lewis T, et al. (2000) Three-dimensional structures of Drosophila melanogaster acetylcholinesterase and of its complexes with two potent inhibitors. Protein Sci 9: 1063–1072.
73. Greenblatt HM, Guillou C, Guenard D, Argaman A, Botti S, et al. (2004) The complex of a bivalent derivative of galanthamine with torpedo acetylcholinesterase displays drastic deformation of the active-site gorge:

implications for structure-based drug design. J Am Chem Soc 126: 15405–15411.
74. Bourne Y, Taylor P, Radic Z, Marchot P (2003) Structural insights into ligand interactions at the acetylcholinesterase peripheral anionic site. EMBO J 22: 1–12.
75. Harel M, Schalk I, Ehret-Sabatier L, Bouet F, Goeldner M, et al. (1993) Quaternary ligand binding to aromatic residues in the active-site gorge of acetylcholinesterase. Proc Natl Acad Sci U S A 90: 9031–9035.
76. Vellom DC, Radic Z, Li Y, Pickering NA, Camp S, et al. (1993) Amino acid residues controlling acetylcholinesterase and butyrylcholinesterase specificity. Biochemistry 32: 12–17.
77. Erdin S, Venner E, Lisewski AM, Lichtarge O (2013) Function prediction from networks of local evolutionary similarity in protein structure. BMC Bioinformatics 14 Suppl 3: S6.
78. Dondoshansky I, Wolf Y (2002) Blastclust (NCBI Software Development Toolkit) Bethesda: NCBI.
79. Nagano N (2005) EzCatDB: the Enzyme Catalytic-mechanism Database. Nucleic Acids Res 33: D407–412.
80. Berman H, Henrick K, Nakamura H (2003) Announcing the worldwide Protein Data Bank. Nat Struct Biol 10: 980.
81. Bashton M, Nobeli I, Thornton JM (2008) PROCOGNATE: a cognate ligand domain mapping for enzymes. Nucleic Acids Res 36: D618–622.
82. Wallace AC, Laskowski RA, Thornton JM (1995) LIGPLOT: a program to generate schematic diagrams of protein-ligand interactions. Protein Eng 8: 127–134.
83. Konagurthu AS, Whisstock JC, Stuckey PJ, Lesk AM (2006) MUSTANG: a multiple structural alignment algorithm. Proteins 64: 559–574.
84. Thompson JD, Higgins DG, Gibson TJ (1994) CLUSTAL W: improving the sensitivity of progressive multiple sequence alignment through sequence weighting, position-specific gap penalties and weight matrix choice. Nucleic Acids Res 22: 4673–4680.
85. Quinlan JR (1993) C4.5: Programs for Machine Learning. San Francisco, CA, USA: Morgan Kaufmann Publishers Inc.
86. Mark H, Eibe F, Geoffrey H, Bernhard P, Peter R, et al. (2009) The WEKA data mining software: an update. SIGKDD Explor Newsl 11: 10–18.
87. R Development Core Team (2008) R: A language and environment for statistical computing. Vienna, Austria: R Foundation for Statistical Computing.

Journal of Bioscience and Bioengineering
VOL. xx No. xx, 1–8, 2014

www.elsevier.com/locate/jbiosc

Control of adhesion of human induced pluripotent stem cells to plasma-patterned polydimethylsiloxane coated with vitronectin and γ-globulin

Ryotaro Yamada,[1] Koji Hattori,[2] Saoko Tachikawa,[1] Motohiro Tagaya,[3] Toru Sasaki,[4] Shinji Sugiura,[2] Toshiyuki Kanamori,[2] and Kiyoshi Ohnuma[1,5,*]

Department of Bioengineering, Nagaoka University of Technology, 1603-1 Kamitomioka, Nagaoka, Niigata 940-2188, Japan,[1] Research Center for Stem Cell Engineering, National Institute of Advanced Industrial Science and Technology (AIST), Tsukuba Central 5th, 1-1-1 Higashi, Tsukuba, 5 Ibaraki 305-8565, Japan,[2] Department of Materials Science and Technology, Nagaoka University of Technology, 1603-1 Kamitomioka, Nagaoka, Niigata 940-2188, Japan,[3] Department of Electrical Engineering, Nagaoka University of Technology, 1603-1 Kamitomioka, Nagaoka, Niigata 940-2188, Japan,[4] and Top Runner Incubation Center for Academia-Industry Fusion, Nagaoka University of Technology, 1603-1 Kamitomioka, Nagaoka, Niigata 940-2188, Japan[5]

Received 19 December 2013; accepted 11 February 2014
Available online xxx

Human induced pluripotent stem cells (hiPSCs) are a promising source of cells for medical applications. Recently, the development of polydimethylsiloxane (PDMS) microdevices to control the microenvironment of hiPSCs has been extensively studied. PDMS surfaces are often treated with low-pressure air plasma to facilitate protein adsorption and cell adhesion. However, undefined molecules present in the serum and extracellular matrix used to culture cells complicate the study of cell adhesion. Here, we studied the effects of vitronectin and γ-globulin on hiPSC adhesion to plasma-treated and untreated PDMS surfaces under defined culture conditions. We chose these proteins because they have opposite properties: vitronectin mediates hiPSC attachment to hydrophilic siliceous surfaces, whereas γ-globulin is adsorbed by hydrophobic surfaces and does not mediate cell adhesion. Immunostaining showed that, when applied separately, vitronectin and γ-globulin were adsorbed by both plasma-treated and untreated PDMS surfaces. In contrast, when PDMS surfaces were exposed to a mixture of the two proteins, vitronectin was preferentially adsorbed onto plasma-treated surfaces, whereas γ-globulin was adsorbed onto untreated surfaces. Human iPSCs adhered to the vitronectin-rich plasma-treated surfaces but not to the γ-globulin-rich untreated surfaces. On the basis of these results, we used perforated masks to prepare plasma-patterned PDMS substrates, which were then used to pattern hiPSCs. The patterned hiPSCs expressed undifferentiated-cell markers and did not escape from the patterned area for at least 7 days. The patterned PDMS could be stored for up to 6 days before hiPSCs were plated. We believe that our results will be useful for the development of hiPSC microdevices.

[**Key words:** Polydimethylsiloxane; Low-pressure air plasma; Microenvironment control; Microdevice; Serum-free culture; Feeder-free culture; iPS cells; Cell adhesion; Competitive adsorption]

Human pluripotent stem cells (hPSCs), including both human embryonic stem cells and human induced pluripotent stem cells (hiPSCs), exhibit infinite self-renewal capacity and pluripotency (1–3). Because hiPSCs and embryonic stem cells generated by somatic cell nuclear transfer contain the donor's genetic information, medical applications of autologous stem cells offer the hope of rejection-free transplantation of tissues and patient-specific drug screening (2,3).

The development of new cell culture devices for patient-specific drug screening using hPSCs requires control of the microenvironment of the cells, including the spatiotemporal distribution of soluble factors, cell–cell interactions, and cell–substrate interactions; and microfabricated devices are increasingly being developed for this purpose (4,5). Polydimethylsiloxane (PDMS) is one of the most popular biocompatible materials for such devices because this elastomer is non-toxic, chemically inert, transparent, and gas permeable (6). For the fabrication of microdevices, PDMS surfaces have often been modified by gas-phase processing methods including plasma treatment (in this paper, plasma refers to low-pressure air plasma, not blood plasma, unless otherwise stated), ultraviolet irradiation, chemical vapor deposition, and sputter coating of metal compounds (7). Plasma treatment is easy to carry out and is used for various purposes, including PDMS–PDMS and PDMS–glass bonding, cleaning PDMS surfaces, and facilitating the coating of surfaces with cell-adhesive extracellular matrix (ECM) proteins (8,9). Therefore, we frequently use plasma treatment in the fabrication of PDMS microdevices for cell culture (10,11).

One of the most fundamental requirements for PDMS microdevices for hPSC applications is that the cells adhere to the PDMS surface, because hPSCs form flat colonies on culture dishes and cannot maintain their pluripotency without adhesion (1,12). Although there have been many studies of adsorption of

* Corresponding author at: Department of Bioengineering, Nagaoka University of Technology, 1603-1 Kamitomioka, Nagaoka, Niigata 940-2188, Japan. Tel./fax: +81 258 47 9454.
E-mail addresses: kohnuma@vos.nagaokaut.ac.jp, kyohnuma@gmail.com (K. Ohnuma).

1389-1723/$ – see front matter © 2014, The Society for Biotechnology, Japan. All rights reserved.
http://dx.doi.org/10.1016/j.jbiosc.2014.02.009

Please cite this article in press as: Yamada, R., et al., Control of adhesion of human induced pluripotent stem cells to plasma-patterned polydimethylsiloxane coated with vitronectin and γ-globulin, J. Biosci. Bioeng., (2014), http://dx.doi.org/10.1016/j.jbiosc.2014.02.009

cell-adhesive and non-cell-adhesive molecules, including ECM components, on biocompatible surfaces (13,14), the mechanism of adhesion remains to be revealed. The study of cell adhesion is complicated by the fact that the culture environment contains unknown amounts of various undefined molecules, including those in the ECM and in serum (15–17). Thus, investigation of how PDMS surface modifications and cell-adhesive and non-cell-adhesive proteins affect hPSC adhesion under defined culture conditions is urgently needed if medical applications of microfabricated devices for hPSCs are to be developed.

Here, we studied the effects of two proteins, vitronectin and γ-globulin, which is one of the most abundant protein in serum, on the adhesion of hiPSCs to plasma-treated and untreated PDMS surfaces under defined culture conditions. We chose vitronectin for three reasons: (i) hPSCs adhere to tissue culture dishes coated with vitronectin (18,19); (ii) vitronectin in serum plays a major role in mediating adhesion of cells to the hydrophilic surface of glass, as reflected in the protein's name ("vitro" = "glass", "nectin" = "cell adhesion molecule") (20,21); and (iii) vitronectin may adsorp well on PDMS, because PDMS, like glass, is rich in Si–O bonds (6). In contrast, γ-globulin (an immunoglobulin) has the opposite adhesion properties and thus can be expected to block adsorption of vitronectin on PDMS for three reasons: (i) although adhesion of PSCs to polymers is mediated by integrins, cadherin, and glycans (16,19,22,23), γ-globulin has not been reported to mediate PSC adhesion; (ii) γ-globulin has a hydrophobic fragment crystallizable (Fc) region that is involved in adsorption on hydrophobic surfaces (7,24); and (iii) PDMS is rich in hydrophobic methylene groups (6).

We investigated the relationships between plasma treatment of PDMS surfaces, vitronectin and γ-globulin adsorption, and hiPSC adhesion under defined culture conditions using hESF9a, a serum- and feeder-free culture medium (25,26); this medium allowed us to study these relationships without masking by undefined factors derived from serum and feeder cells. We used the results of our initial investigations to pattern a PDMS surface with hiPSCs.

MATERIALS AND METHODS

Culture and subculture of hiPSCs Two hiPSC cell lines, 201B7 (2) and 253G1 (27), were obtained from RIKEN BRC Cell Bank (Tsukuba, Japan) through the National BioResource Project for the Ministry of Education, Culture, Sports, Science and Technology, Japan. The 201B7 line was used unless otherwise stated. For all experiments, hiPSCs cultured in KSR-based medium on mouse embryonic fibroblast feeder cells were transferred to serum- and feeder-free culture conditions in hESF9a medium (11,25) on dishes coated with 2 μg/mL fibronectin from bovine blood plasma (F-1141, Sigma–Aldrich, St. Louis, MO, USA) and were passaged at least once before use (11,26). For subculturing, the cells were detached from the culture dish by using 0.2–0.5 U/mL dispase (17105-041, Life Technologies, Grand Island, NY, USA) in hESF9a medium and replated in hESF9a medium with 5 μM ROCK inhibitor (Y-27632, Wako Pure Chemical Industries, Osaka, Japan), which blocks dissociation-induced apoptosis of hPSCs (12). The hESF9a medium was changed daily. For the adhesion experiments, hiPSCs were dissociated into single cells by incubation and trituration in 0.02% (w/w) ethylenediaminetetraacetic acid (EDTA) in $PBS^{-/-}$ and then plated in hESF9a solution with 5 μM ROCK inhibitor.

Preparation and plasma treatment of PDMS surfaces PDMS prepolymer and curing agent (Sylgard 184, Dow Corning, Midland, MI, USA) were thoroughly mixed at a 10:1 weight ratio. To make PDMS sheets, we poured the mixture between two polyethylene terephthalate films separated with 0.5 mm rubber spacers and cured it in an oven at 120°C for 2 h. To make perforated masks, we perforated the sheet with 2-mm-diameter holes by using a hole punch. The resultant 0.5-mm-thick PDMS sheets and perforated masks were rinsed with ethanol and sterilized at 160°C for 2 h.

PDMS sheets with or without a perforated mask were hydrophilized by treatment with a low-pressure air plasma for 60 s (YHS-R, Sakigake-Semiconductor Co., Kyoto, Japan) after 5 min under vacuum (ultimate vacuum, 2 Pa; TA150XA, Tasco, Osaka, Japan). Between 30 min and 1 h later (unless otherwise stated), the perforated mask was removed, if one was used, and the PDMS sheet surface was coated with 5.5 mg/mL rabbit γ-globulin (011-000-002, Jackson ImmunoResearch Laboratories, Inc., West Grove, PA, USA), 0.6 $\mu g/cm^2$ human blood plasma–derived vitronectin (2349-VN, R&D Systems), or both, and the coated sheet was incubated overnight at 37°C.

Contact angle measurement and Fourier transform infrared spectroscopy The water contact angle of the PDMS surfaces was analyzed in air by the sessile drop method using a droplet of distilled water (2 μL). Droplets were photographed with a digital camera (CX3, Ricoh, Tokyo, Japan), and the angles were estimated by half-angle contact methods using Image J software (NIH, Bethesda, MD, USA).

For Fourier transform infrared (FT-IR) spectroscopy, a PDMS thin film was prepared as reported before (28). Briefly, 0.1 g of a mixture of PDMS was dissolved in 30 mL of chloroform, and the solution was spin-coated (3000 rpm, 20 s) onto an oxidized Si(111) substrate. The resulting PDMS film was cured at 65°C for 12 h. The surface chemical bonding of the PDMS thin film was analyzed by FT-IR spectroscopy (Nicolet, Thermo Fisher Scientific). Spectra were accumulated from 32 scans at a resolution of 1.0 cm^{-1} in transmittance mode in the wavenumber range between 4,000 and 400 cm^{-1}.

Cell attachment assay and immunostaining Attached living cells were stained with 1 μM calcein AM (Dojindo, Kumamoto, Japan), a fluorescent dye that can be transported into living cells, for 20 min at 37°C. For immunostaining of the surface of PDMS coated with proteins, the PDMS surface was rinsed with PBS containing 0.5 mM $CaCl_2$ and 0.5 mM $MgCl_2$ ($PBS^{+/+}$), fixed in 4% formaldehyde (Sigma–Aldrich) with 0.5 mM $MgCl_2$ and 0.5 mM $CaCl_2$, and reacted with primary antibodies overnight; the primary antibodies were then visualized with secondary antibodies (Table S1). The antibodies were diluted in $PBS^{+/+}$ containing 10 mg/mL bovine serum albumin. For immunocytochemistry, hiPSCs plated on conventional culture dishes were rinsed with $PBS^{+/+}$, fixed in 4% formaldehyde with 0.5 mM $MgCl_2$ and 0.5 mM $CaCl_2$, permeabilized, blocked with $PBS^{+/+}$ containing 0.2% Triton X-100 and 10 mg/mL bovine serum albumin, and reacted with primary antibodies, which were visualized with secondary antibodies (Table S1). The antibodies were diluted in $PBS^{+/+}$ containing 0.2% Triton X-100 and 10 mg/mL bovine serum albumin. Nuclei were stained with 0.4 μM 4′,6-diamidino-2-

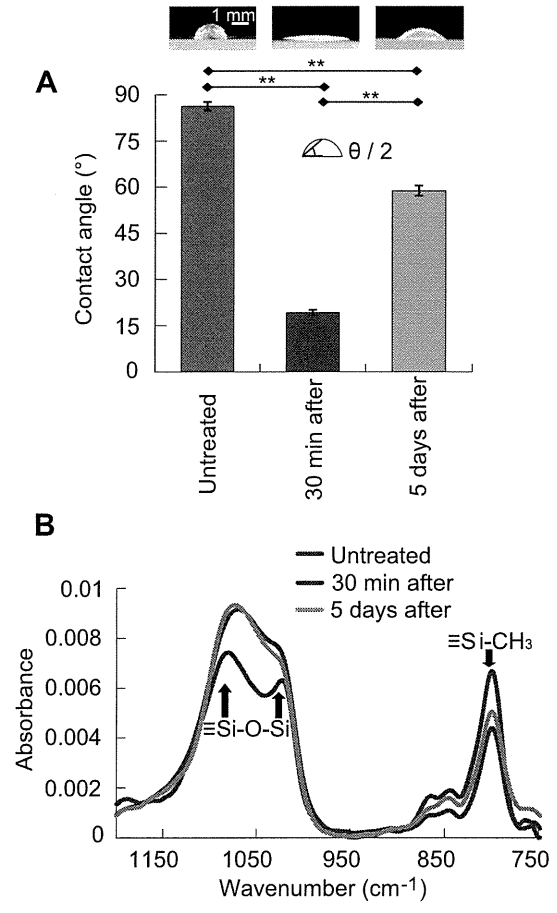

FIG. 1. Effects of plasma treatment of PDMS surfaces. (A) Contact angle (θ) of water. Data are means ± SE ($n = 5$). ** $P < 1 \times 10^{-10}$, Tukey's multiple comparison. Insets are photographs of 2 μL water droplets. (B) FT-IR absorbance spectra of PDMS before plasma treatment (blue) and 30 min (red) or 5 days (green) after 60-s plasma treatment. The arrows represent functional groups whose absorbances were changed by plasma treatment. (For interpretation of the references to colour in this figure legend, the reader is referred to the web version of this article.)

Please cite this article in press as: Yamada, R., et al., Control of adhesion of human induced pluripotent stem cells to plasma-patterned polydimethylsiloxane coated with vitronectin and γ-globulin, J. Biosci. Bioeng., (2014), http://dx.doi.org/10.1016/j.jbiosc.2014.02.009

phenylindole (DAPI, Wako). Fluorescence micrographs were obtained with a BZ-8100 fluorescence microscope (Keyence, Osaka, Japan) and analyzed with Image J software (NIH).

RESULTS

Effects of plasma treatment on PDMS surface structure To determine how plasma treatment affected PDMS hydrophilicity, we measured the contact angle of a 2 μL water droplet and found that 30 min after a 60-s plasma treatment, the contact angle (19°) was significantly lower than the angle before treatment (86°, Fig. 1A), indicating that the PDMS surface had been hydrophilized by the plasma treatment. The contact angles after 15- and 60-s treatments were the same, and the angle was stable during the period from 30 min to 2 h after treatment (Fig. S1). The contact angle increased gradually, and by 5 days after treatment, the angle had recovered to approximately 70% (59°/86°) of that for the untreated surface (Figs. S1 and 1A), suggesting the hydrophobicity of the PDMS surface had been restored. On the basis of these results, we coated PDMS with vitronectin, γ-globulin, or both during the period between 30 min and 1 h after plasma treatment, unless otherwise stated.

Next we measured the absorbance of a PDMS thin film by means of FT-IR (Fig. 1B). Plasma treatment of PDMS caused a noticeable decrease in the absorbance bands at 800 cm^{-1} derived from CH_3 rocking and ≡Si–C stretching vibrations, indicating a decrease in the number of methyl groups. In contrast, two bands, centered at 1,026 and 1,070 cm^{-1} and attributable to asymmetric ≡Si–O–Si stretching vibrations, were increased by plasma treatment, indicating that the CH3–Si–O groups in PDMS underwent transformation to O–Si–O groups. Taken together, the changes in the FT-IR spectra suggest that a siliceous layer formed at the surface of PDMS film as a result of plasma treatment.

Adsorption of vitronectin on and adhesion of hiPSCs to plasma-treated and untreated PDMS surfaces We next investigated how vitronectin mediated hiPSC adhesion to the PDMS surfaces. It is well known that many types of adhesive cells can be cultured on a plasma-treated hydrophilic polystyrene dish, generally referred to as a tissue culture treated dish, but not on an untreated hydrophobic polystyrene dish. Moreover, formation of a siliceous layer by plasma treatment may facilitate hiPSC adhesion to PDMS surfaces coated with vitronectin, which mediates cell–glass adhesion (20). Thus we hypothesized that vitronectin coating would enable hiPSCs to adhere to plasma-treated PDMS surfaces but not to untreated PDMS surfaces. To test this hypothesis, we coated untreated and plasma-treated PDMS surfaces with vitronectin. Immunostaining with anti-

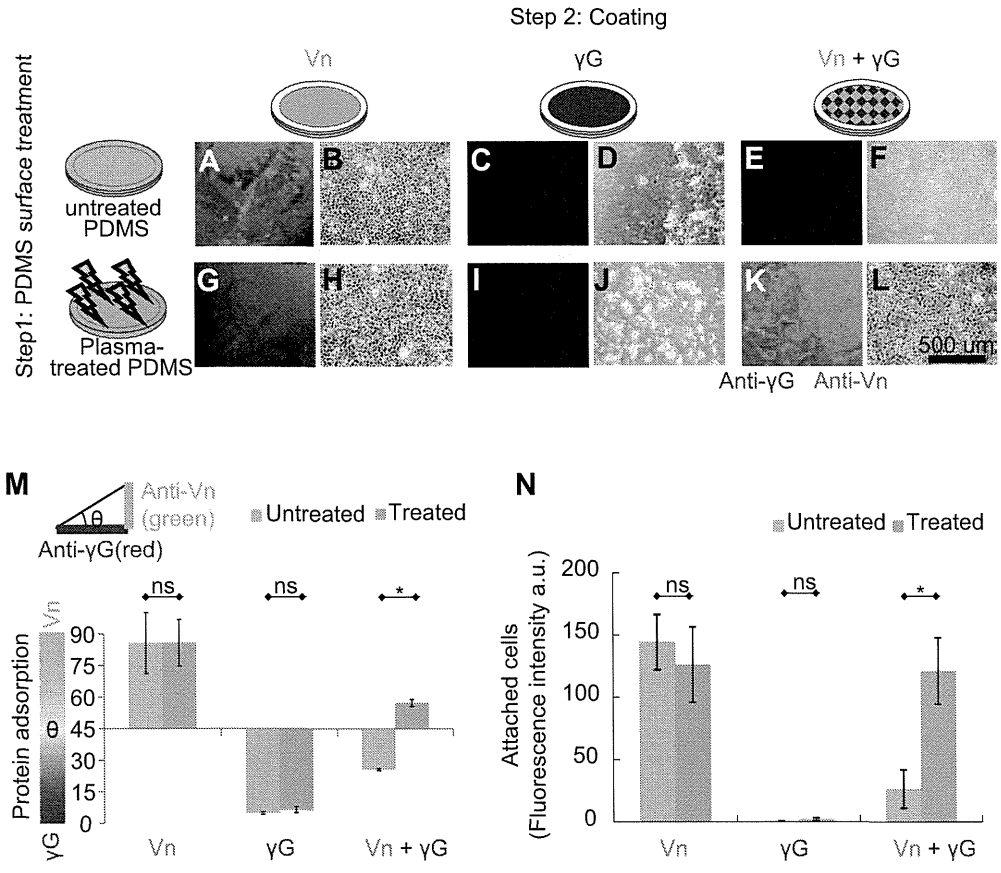

FIG. 2. Vitronectin (Vn) and γ-globulin (γG) adsorption on and hiPSC adhesion to plasma-treated and untreated PDMS surfaces. Untreated (A–F) and plasma-treated (G–L) PDMS surfaces coated with vitronectin alone (A, B, G, H), γ-globulin alone (C, D, I, J), or a mixture of vitronectin and γ-globulin (E, F, K, L). (A, C, E, G, I, K) Double immunostaining of PDMS surfaces with anti-vitronectin (green) and anti-γ-globulin (red) antibodies. (B, D, F, H, J, L) Phase-contrast micrographs of hiPSCs cultured in hESF9a. (M) Adsorption ratio (θ) of vitronectin and γ-globulin on PDMS. $\theta = \tan^{-1}$(anti – vitronectin (green flourescence)/anti-γ-gloubulin (red flourescence)). Fluorescence intensity is given in arbitrary units. Theta is <45° where the red fluorescence (γ-globulin) is greater than the green fluorescence (vitronectin), and θ is >45° where the green florescence (vitronectin) is greater than the red fluorescence (γ-globulin). Data are means ± SE ($n = 3$). *$P < 0.05$, ns: not significant, Holm's multiple comparisons. (N) Attached cells on a 2-mm circle estimated by means of staining with calcein AM. PDMS surfaces were coated with vitronectin alone, both vitronectin and γ-globulin, or γ-globulin alone. Data are means ± SE ($n = 3$). *$P < 0.05$, ns: not significant, Holm's multiple comparisons. (For interpretation of the references to colour in this figure legend, the reader is referred to the web version of this article.)

Please cite this article in press as: Yamada, R., et al., Control of adhesion of human induced pluripotent stem cells to plasma-patterned polydimethylsiloxane coated with vitronectin and γ-globulin, J. Biosci. Bioeng., (2014), http://dx.doi.org/10.1016/j.jbiosc.2014.02.009

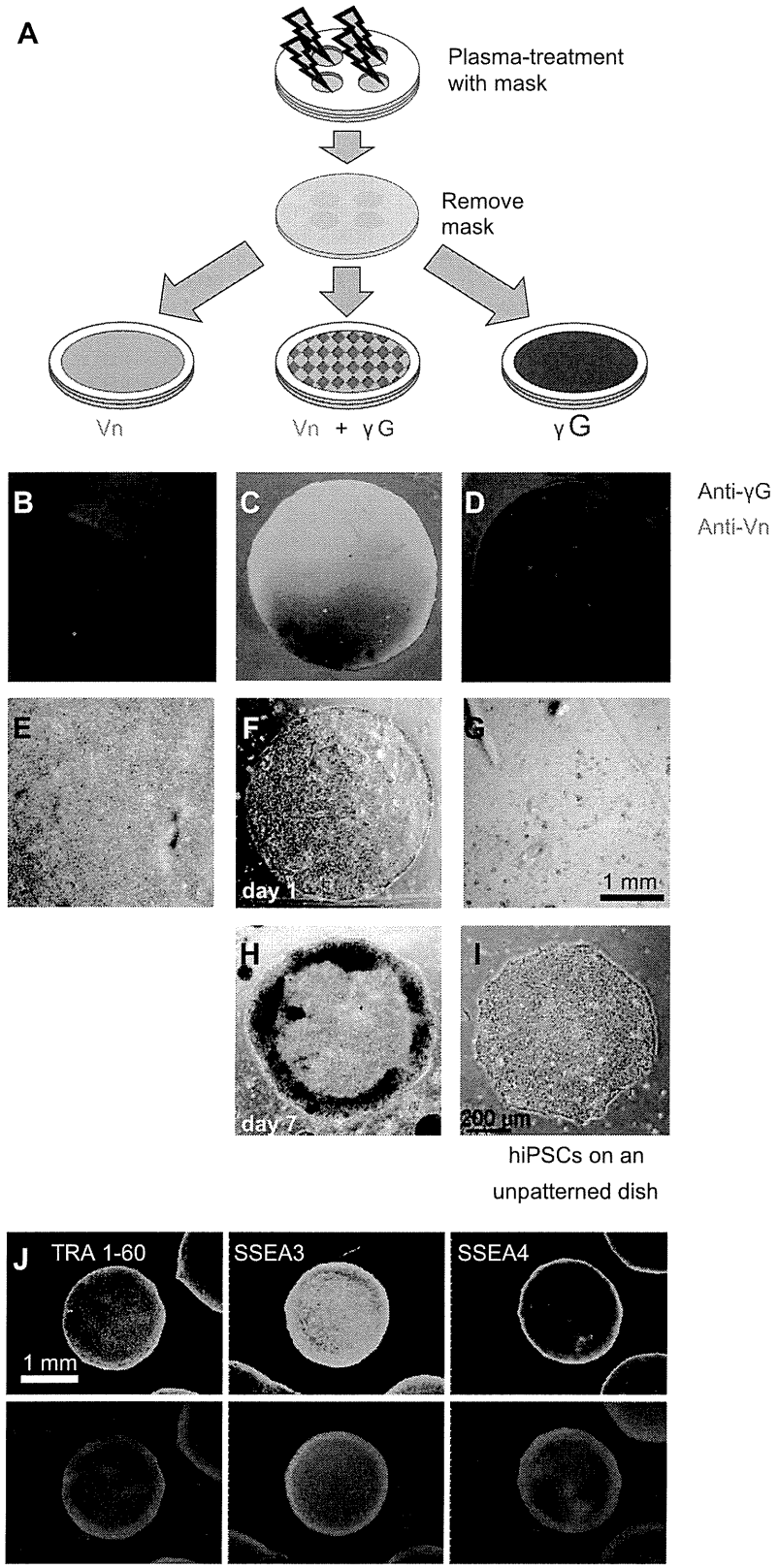

FIG. 3. Patterning of hiPSCs by plasma patterning of PDMS surfaces and subsequent coating with vitronectin (Vn) and γ-globulin (γG). (A) Schematic of preparation of plasma-patterned, protein-coated PDMS. PDMS sheets covered with a perforated mask (2-mm-diameter holes) were treated with plasma and then coated with vitronectin alone (B, E), a mixture of γ-globulin and vitronectin (C, F, H), or γ-globulin alone (D, G). (B–D) Immunostaining of PDMS sheets coated with anti-vitronectin (green) and anti-γ-globulin antibodies (red). (E–H) Phase-contrast micrographs of hiPSCs cultured for 1 day (E–G) or 7 days (H) in a defined culture medium. (B–H) The scales are the same. (I) Phase-contrast micrograph of an hiPSC colony without feeder cells on an unpatterned culture dish. (J) Immunostaining for undifferentiated-cell marker antibodies 4 days after cell plating: anti-TRA 1-60 antibody (green), anti-SSEA3 antibody (green), and anti-SSEA4 antibody (green). Nuclei are stained with DAPI (blue, lower panels). (For interpretation of the references to colour in this figure legend, the reader is referred to the web version of this article.)

Please cite this article in press as: Yamada, R., et al., Control of adhesion of human induced pluripotent stem cells to plasma-patterned polydimethylsiloxane coated with vitronectin and γ-globulin, J. Biosci. Bioeng., (2014), http://dx.doi.org/10.1016/j.jbiosc.2014.02.009

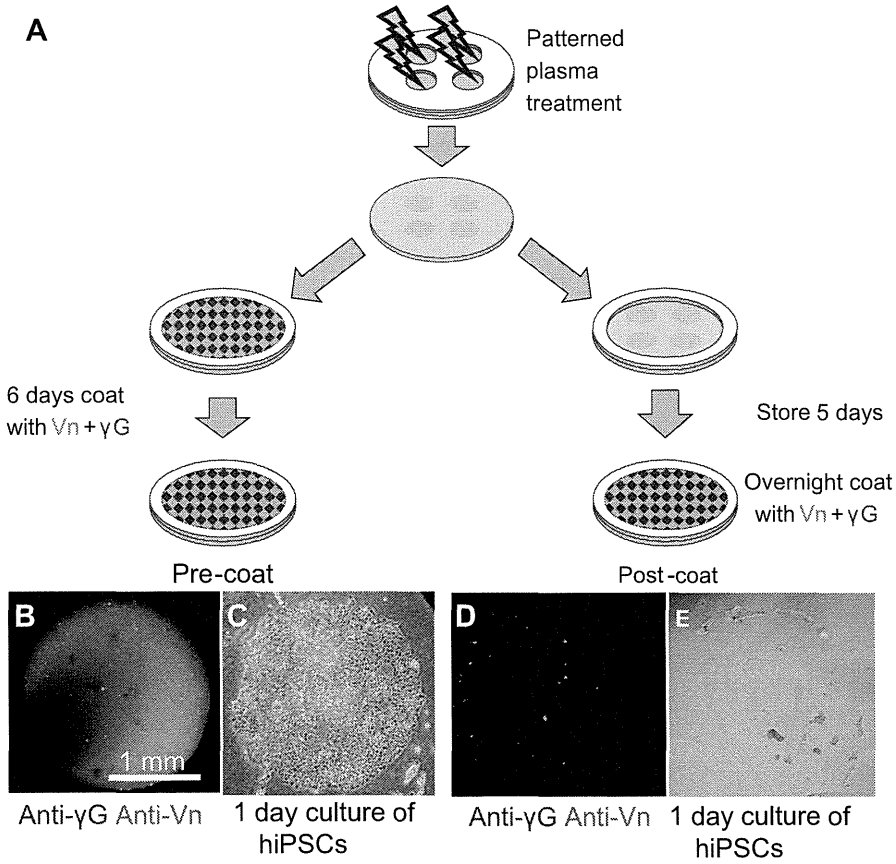

FIG. 4. Storability of plasma-patterned, protein-coated PDMS surfaces. (A) Schematic of pre-coat and post-coat storage experiments. Masked PDMS was treated with plasma and then either pre-coated with a mixture of γ-globulin (γG) and vitronectin (Vn) approximately 30 min after plasma treatment and stored for 6 days (left) or post-coated with the protein mixture 5 days after plasma treatment (right). Immunostaining of pre-coated (B) and post-coated (D) PDMS by anti-vitronectin (green) and anti-γ-globulin antibodies (red). Phase-contrast micrographs of hiPSCs cultured on pre-coated (C) and post-coated (E) PDMS for 1 day in a defined culture medium. (For interpretation of the references to colour in this figure legend, the reader is referred to the web version of this article.)

vitronectin antibodies showed that vitronectin was adsorbed on both plasma-treated and untreated PDMS surfaces (Figs. 2A, G, M and S2) and that hiPSCs adhered to both surfaces (Figs. 2B, H, N and S2). Thus, these results did not support our initial hypothesis.

Effect of γ-globulin on hiPSC adhesion to untreated PDMS surfaces We suspected that a blocking factor was needed to prevent vitronectin adsorption on the untreated hydrophobic PDMS surface. For this purpose, we chose γ-globulin, which has a hydrophobic Fc region and has not been reported to mediate PSC adhesion (16,19,22,23). We hypothesized that γ-globulin would adsorb preferentially to the untreated, hydrophobic PDMS surface and would thus block cell adhesion. To test this hypothesis, we coated untreated and plasma-treated PDMS surfaces with a mixture of vitronectin and γ-globulin. Immunostaining showed that bright red staining (red fluorescence was stronger than green fluorescence) on the untreated PDMS surface and bright green staining (green fluorescence was stronger than red fluorescence) on the plasma-treated PDMS surface, indicating γ-globulin and vitronectin were adsorbed preferentially on the untreated and plasma-treated PDMS surfaces, respectively (Figs. 2E, K, M and S2). Human iPSCs adhered to the plasma-treated vitronectin-rich surface but not to the untreated γ-globulin-rich surface (Figs. 2F, L, N and S2). These results supported our second hypothesis. Interestingly, coating with γ-globulin alone resulted in adsorption of γ-globulin on both untreated and plasma-treated PDMS surfaces, and hiPSCs did not adhere to either surface (Figs. 2C, D, I, J, M, N and S2). These results suggest that γ-globulin blocked adsorption of vitronectin on the untreated PDMS surface and thus prevented hiPSC adhesion.

Patterning of hiPSCs on plasma-patterned PDMS surfaces coated with vitronectin and γ-globulin We speculated that our results might be useful for generating hiPSC patterning on PDMS surfaces, so we carried out the following experiments. We patterned a PDMS surface by applying a PDMS mask perforated with 2-mm-diameter holes and then treating the masked surface with plasma. After removal of the mask, the plasma-patterned surface was coated with vitronectin, γ-globulin, or both (Fig. 3A). Immunostaining showed that when the patterned surface was treated with either vitronectin alone or γ-globulin alone, the protein was adsorbed onto the entire surface (Fig. 3B, D). In contrast, when the patterned surface was treated with a mixture of the two proteins, immunostaining showed bright green staining in the circular (plasma-treated) areas and bright red staining in the surrounding (untreated) areas as shown in Fig. 2E, K, indicating that vitronectin and γ-globulin were preferentially adsorbed onto the plasma-treated and untreated areas, respectively (Fig. 3C). Human iPSCs adhered to the entire surface of PDMS coated with vitronectin alone but did not adhere to the surface coated with γ-globulin alone (Fig. 3E, G). In contrast, treatment of the patterned PDMS with a mixture of vitronectin and γ-globulin allowed hiPSCs to adhere to the plasma-treated circular areas (Fig. 3F), and the hiPSCs remained in those areas for at least 7 days (Fig. 3H). The morphology of patterned hiPSCs appeared to be that of normal hiPSC colonies (Fig. 3I); the

Please cite this article in press as: Yamada, R., et al., Control of adhesion of human induced pluripotent stem cells to plasma-patterned polydimethylsiloxane coated with vitronectin and γ-globulin, J. Biosci. Bioeng., (2014), http://dx.doi.org/10.1016/j.jbiosc.2014.02.009

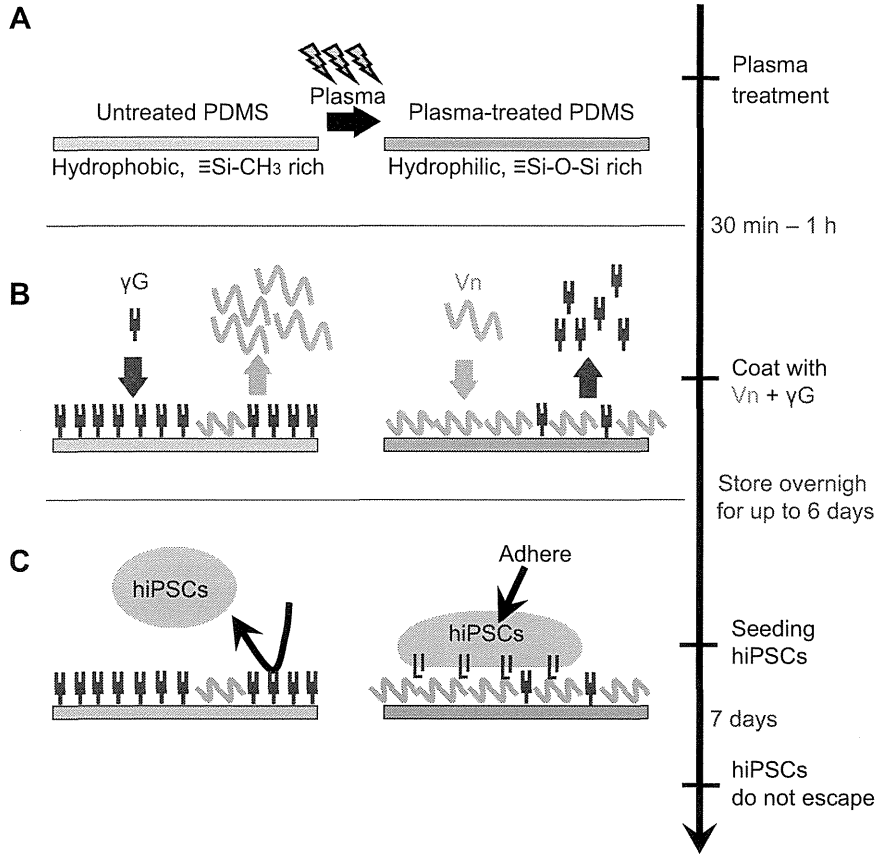

FIG. 5. Schematic of experimental results. (A) Plasma treatment of the PDMS surfaces decreased the number of methyl groups and increased the number of siloxane bonds, resulting in the formation of a siliceous surface (thus increasing hydrophilicity). (B) Coating PDMS with a mixture of vitronectin (Vn) and γ-globulin (γG), but not with either protein individually, resulted in adsorption of γ-globulin on the untreated PDMS surface and adsorption of vitronectin on the plasma-treated PDMS surface. (C) Human iPSCs adhered to the vitronectin-rich plasma-treated surfaces but not to the γ-globulin-rich untreated surfaces; this difference resulted in hiPSCs patterning. Treating the surfaces with vitronectin and γ-globulin prior to storage permitted retention of the protein pattern for at least 6 days of storage. The hiPSCs did not escape from the patterned area for at least 7 days.

colonies were tightly packed and flat (monolayer) and consisted of cells with large nuclei and scant cytoplasm (1,2,26). Because the cells kept proliferating without escaping from the plasma-treated area, the edges of the colonies became thick (multilayer) and appeared dark under a phase-contrast microscope on day 7 (Fig. 3H). Immunostaining revealed that the patterned hiPSCs expressed undifferentiated-cell markers TRA 1-60, SSEA3, and SSEA4 (Fig. 3J). We obtained the same results by using another hiPSC line, 253G1 (Fig. S3). These results suggest that our method can be used to prepare hiPSCs on plasma-patterned PDMS surfaces.

Storage of plasma-patterned PDMS before plating of cells Next we determined whether the cell patterning would form if the PDMS was stored for several days after plasma patterning. It would be convenient if patterned PDMS sheets could be prepared several days before cells were plated because this would enable batch production of many PDMS plates of the same quality. Although the plasma-hydrophilized surface of the PDMS recovered its hydrophobicity 5 days after plasma treatment (Fig. 1A), the hiPSCs retained the pattern for 7 days (Fig. 3H), which suggests that coating the surface with vitronectin and γ-globulin 30 min after plasma treatment enabled retention of the plasma pattern for 7 days. To test this, we evaluated two preparation methods: a pre-coat method and a post-coat method. In the pre-coat method, PDMS surfaces were plasma-patterned on day 0, the patterned PDMS was coated with vitronectin and γ-globulin 30 min after plasma treatment, and the coated PDMS was then stored in a CO_2 incubator for 6 days (Fig. 4A). In the post-coat method, the PDMS surfaces were plasma-patterned on day 0, stored in a CO_2 incubator for 5 days, and coated with vitronectin and γ-globulin for overnight (Fig. 4A). Under the pre-coat conditions, vitronectin adhered to the circular areas, which were surrounded by γ-globulin, and the hiPSCs adhered to the circular areas (Fig. 4B, C). In contrast, the entire post-coated PDMS surface adsorbed γ-globulin, and hiPSCs did not adhere to the surface (Fig. 4D, E). These results suggest that vitronectin and γ-globulin coating of the plasma-patterned surface suppressed recovery of hydrophobicity and thus enabled retention of the patterning.

DISCUSSION

There are many reports describing chemical modifications of PDMS surfaces including photo-oxidation and plasma treatment (7–9,29,30). In this study, we used plasma treatment, during which a reaction involving a collision between an electron and O_2 generates a singlet oxygen atom, which etches the PDMS surface (29). FT-IR analysis of the PDMS surface before and after plasma treatment indicated that plasma exposure resulted in the formation of ≡Si–O–Si≡ groups by oxidation of ≡Si–CH_3 by singlet oxygen radical species. Oxidization of PDMS film surfaces by exposure to vacuum ultraviolet light (λ = 172 nm) has been reported to reduce the number of ≡Si–CH_3 groups and subsequently increase the numbers of ≡Si–OH and ≡Si–O–Si≡ groups on the surfaces (28). In our present study, the absorbance band due to ≡Si–O–Si≡ in

Please cite this article in press as: Yamada, R., et al., Control of adhesion of human induced pluripotent stem cells to plasma-patterned polydimethylsiloxane coated with vitronectin and γ-globulin, J. Biosci. Bioeng., (2014), http://dx.doi.org/10.1016/j.jbiosc.2014.02.009